A New Four-Component L*-dependent Model for Radial Diffusion based on Solar Wind and Magnetospheric Drivers of ULF Waves

Kyle R. Murphy[1,2,3], Jasmine Sandhu[2], I. Jonathan Rae[2], Thomas Daggitt[4,5], Sarah Glauert[4], Richard B. Horne[4], Clare E. J. Watt[2], Sarah Bentley[2], Adam Kellerman[6], Louis Ozeke[7], Alexa J. Halford[8], Sheng Tian[9,10], Aaron Breneman[8], Leonid Olifer[7], Ian R. Mann[2,7], Vassilis Angelopoulos[6], John Wygant[10]

Affiliations:

1. Self - Independent Researcher, Thunder Bay, ON, Canada
2. Department of Maths, Physics and Electrical Engineering, Northumbria University, Newcastle Upon Tyne, United Kingdom
3. Department of Physics, Lakehead University, Thunder Bay, ON, Canada
4. British Antarctic Survey, Cambridge, UK
5. Department of Applied Mathematics and Theoretical Physics, University of Cambridge, Cambridge, UK
6. Department of Earth, Planetary, and Space Sciences, University of California, Los Angeles, CA, USA
7. Department of Physics, University of Alberta, Edmonton, Alberta, Canada
8. NASA Goddard Spaceflight Center, Greenbelt, MD, USA
9. Department of Atmospheric and Oceanic Sciences, University of California Los Angeles, CA, Los Angeles, USA
10. School of Physics and Astronomy, University of Minnesota, Minneapolis, MN, USA

Key Words: ulf waves, radial diffusion, radiation electron belt dynamics, L*, solar wind driving, geomagnetic activity

Abstract

Waves which couple to energetic electrons are particularly important in space weather, as they drive rapid changes in the topology and intensity of Earth's outer radiation belt during geomagnetic storms. This includes Ultra Low Frequency (ULF) waves that interact with electrons via radial diffusion which can lead to electron dropouts and rapid acceleration and inward transport of electrons during. In radiation belt simulations, the strength of this interaction is specified by ULF wave radial diffusion coefficients. In this paper we detail the development of new models of electric and magnetic radial diffusion coefficients derived from in-situ observations of the azimuthal electric field and compressional magnetic field. The new models use L^* as it accounts for adiabatic changes due to the dynamic magnetic field coupled with an optimized set of four components of solar wind and geomagnetic activity, B_z, V, P_{dyn} and $Sym\text{-}H$, as independent variables (inputs). These independent variables are known drivers of ULF waves and offer the ability to calculate diffusion coefficients at a higher cadence then existing models based on Kp. We investigate the performance of the new models by characterizing the model residuals as a function of each independent variable and by comparing to existing radial diffusion models during a

quiet geomagnetic period and through a geomagnetic storm. We find that the models developed here perform well under varying levels of activity and have a larger slope or steeper gradient as a function of L^* as compared to existing models (higher radial diffusion at higher L^* values).

Plain Language Summary

The outer radiation belt is a region of space comprising highly energetic electrons. During periods of extreme space weather, the number and energy of these electrons can rapidly vary. During these periods as the electron energies and numbers become enhanced, they can pose a threat to satellite and space infrastructure. While we have an excellent understanding of the physical processes which drive radiation belt electron dynamics, we still have a limited ability to model and forecast radiation belt dynamics; this is a result of the complexity of Earth's radiation belt system. One of the key processes controlling radiation belt dynamics is Ultra Low Frequency (ULF) wave radial diffusion. In this work we detail the development a new model quantifying the strength of Ultra Low Frequency (ULF) wave radial diffusion in the outer radiation belt utilizing space base observations of the electric and magnetic fields in Earth's magnetosphere. Accurately quantifying ULF wave radial diffusion is fundamental to understanding radiation belt dynamics and any improvement or refinements in radial diffusion models can help to provide a better understanding of the complex radiation belt system and importantly improve hindcasts, nowcasts, and forecasts.

1 Introduction

The Earth's outer radiation belt is a toroidal region between ~2-8 R_E comprising energetic electrons from hundreds of keV to several MeV (Mauk et al., 2013). Periods of elevated solar activity, such as coronal mass ejections, corotating interaction regions, dynamic solar wind, and interplanetary shocks can drive increased geomagnetic activity leading to rapid changes in the flux of energetic electrons and enhancements of the terrestrial ring current (e.g., Kanekal & Miyoshi, 2021). These periods of enhanced geoeffective solar wind are referred to as geomagnetic storms. During these storms the enhanced fluxes of the radiation belt can be dangerous for human and robotic space activity as well as causing damage to sensitive spacecraft systems (e.g., Baker 2001; Cassak et al., 2017).

Though the outer radiation belt was discovered over half a century ago (Van Allen & Frank, 1959), our understanding of, and ability to model and forecast its dynamics remains somewhat limited. This is not a result of a lack of understanding of the processes which drive radiation belt dynamics but instead is due to the complexity and variability of the overall system, from the sources and sinks of electrons and wave-particle interactions coupling to these electrons, to the cross-coupling with other magnetospheric regimes such as the magnetopause (e.g., Borovsky & Valdivia, 2018; Halford et al., 2022; J. Rae et al., 2022). During storms, the dynamics of the radiation belt are controlled by a variety of physical processes leading to loss, transport, and acceleration of electrons. For instance, magnetopause shadowing (Staples et al., 2022; West et al. 1972) coupled with outward radial diffusion driven by Ultra Low Frequency (ULF) waves (e.g., Turner et al., 2012) can drive rapid losses of electrons. At the same time wave-particle interactions driven by Very Low Frequency (VLF) Chorus and Hiss waves (e.g., Breneman et al., 2015; Halford et al., 2022; O'Brien et al., 2004), electromagnetic ion cyclotron waves (EMIC) (e.g., Bingley et al., 2019; Bruno et al., 2022), ULF waves (e.g., Brito et al., 2015; Rae et al. 2018), and kinetic Alfven (e.g., Chaston et al., 2018) waves can enhance electron precipitation across a wide range of energies leading to a loss of radiation belt electrons. Further, enhanced convection and substorm injections can replenish lower energy electrons providing pathway for the excitation of whistler mode chorus which can rapidly accelerate electrons to relativistic (several MeV) energies (Horne 2003; Horne and Thorne 1998; Horne et al. 2005; Thorne et al., 2013) creating peaks in electron phase space density (Reeves et al., 2013). ULF (Ozeke et al. 2014) waves can further rapidly accelerate and transport these lower energy seed electrons to MeV energies via ULF wave radial diffusion.

The evolution of the radiation belt is controlled by the sum of the effects of the physical processed described above, and whose strengths varies throughout any given storm leading to a variety of responses. For example, while loss processes typically dominate during the early part of geomagnetic storms (Murphy et al. 2018), the relative strength of these processes varies through the course of a storm and for storm to storm. This variation can lead to striking differences in the topology of the outer radiation belt such as the formation of multiple outer radiation belts (Baker et al. 2013). Following this initial period of loss, the outer radiation belt typically experiences a short period of rapid acceleration (Murphy et al. 2018). However, the dominant process controlling this acceleration can also vary from storm to storm (Ma et al., 2018) and though this period of acceleration is typical of all storms, the amount of acceleration varies (Murphy et al. 2020). This delicate balance between loss, acceleration and transport processes is often referred to as a competition. However, it's more a symphony than a

competition; an orchestra of physical processes of varying magnitudes working in concert to shape the topology of the radiation belt through the course of a geomagnetic storm.

Fully understanding the dynamics of the outer radiation belt requires at least three key steps. First we need to be able to quantify the strength of physical processes controlling these dynamics. Second, we need to assess how the varying strength of the processes act together to impact the overall topology of the outer radiation belt. Finally, we need understand the pre-existing state of the belts (e.g. initial conditions), and the availability or lack thereof of various source populations (e.g., boundary conditions) through the course of a storm.

ULF wave radial diffusion is a key physical processes controlling the dynamics of the outer radiation belt (Schulz & Lanzerotti, 1974). Depending on the gradient of electron phase space density in the outer radiation belt ULF wave radial diffusion can drive either rapid loss or rapid acceleration of radiation belt electrons (Figure 16 of Li & Hudson, 2019; Figure 3 of Turner et al., 2012) across a wide range of energies. In this paper we detail the development of a new model for electric and magnetic ULF wave radial diffusion coefficients, D_{LL}^{E} and D_{LL}^{B}, driven by both solar wind input and geomagnetic activity and addressing the first of the three steps described above. This is a more detailed approach which allows the model to account for variability in radial diffusion as well as allowing the model to have a higher cadence than existing models based on a single low resolution independent variable Kp. The new model is derived from in-situ observations of the azimuthal electric field and compressional magnetic field which are used to create a database of satellite-derived D_{LL}^{E} and D_{LL}^{B}s. Using this database, we further characterize the performance of the models and identify, quantify, and remove biases in the model to provide an overall improved model of both D_{LL}^{E} and D_{LL}^{B}. Accurately quantifying ULF wave radial diffusion is fundamental to understanding the spatio-temporal dynamics of the radiation belt. Thus, any improvement or refinements in the quantification of the rates of ULF radial diffusion coefficients can increase the fidelity of radiation belt simulations. This in turn can provide better hindcasts, nowcasts, and forecasts of the outer radiation belt, and thus deliver a better understanding of the complex system of wave-particle interaction processes described above and which act in concert to produce the observed radiation belt response.

In the subsequent sections we detail the data and methodology used to calculate satellite-derived ULF wave radial diffusion coefficients. This is followed by a description of the development of the D_{LL}^{E} and D_{LL}^{B} models, including a parametric study to identify the best set of solar wind and geomagnetic variables to use, and an investigation of the performance and bias of the new models as a function of independent variable. The new D_{LL}^{E} and D_{LL}^{B} models are then compared to existing models of ULF wave radial diffusion during an interval of quiet geomagnetic activity as well as during a geomagnetic storm. These results are then summarized and we conclude with future work and potential directions for future research.

2 Data and Methodology

In this work we utilize in-situ observations of ULF wave fluctuations to develop an analytic model of ULF wave electric and magnetic radial diffusion coefficients (D_{LL}^{E} and D_{LL}^{B}) which can be used in radiation belt

simulations. To achieve this, observations of the inner-magnetosphere magnetic and electric field from the Time History of Events and Macroscale Interactions During Substorms (THEMIS) probes (Angelopoulos, 2008; Sibeck & Angelopoulos, 2008), the two Van Allen Probes (Mauk et al., 2013), and magnetic field data from the Operational Environment 15 (NOAA GOES-15) satellite (Singer et al., 1996) from a similar time period are used (2012-2020). From these data, we develop a database of ULF wave power spectral density (PSD), calculate satellite-derived D_{LL}^{E} and D_{LL}^{B} from the PSD database, and subsequently derive an analytic model of both D_{LL}s. Supporting Information Table S1 lists the satellites, time period, instruments, and observables used to calculate the electric and magnetic ULF wave PSD. These PSD are then used to estimate the magnetic and electric D_{LL}s. In addition to the in-situ magnetospheric observations, we also use the OMNI dataset (King & Papitashvili, 2005), and the SpacePy (Niehof et al., 2022) and International Radiation Belt Environment Modeling (IRBEM) libraries (Boscher et al., 2022) to parameterize the derived PSD and D_{LL}s as function of prevailing solar wind, geomagnetic conditions, and third adiabatic invariant L^*. In this study we use the TS05 magnetic field model (Tsyganenko & Sitnov, 2005) to derive L^* using the (IRBEM) library (Boscher et al., 2022) assuming a 90° local pitch angle. The OMNI data set and L^* are used as independent variables (or inputs) to train our radial diffusion models (Section 3). Note, we only use GOES West as it is closer to the magnetic equator then GOES East and therefore provides a better estimate of equatorial ULF wave PSD. This requirement, along with ensuring that the missions overlap in time, means that only GOES-15 is used in this study. Further, we use THEMIS A, D, and E as during the period of interest the other two probes are orbiting the moon. Finally, we use L^* rather then L or radial distance as it more accurately characterizes the topological state of the outer radiation belt as it accounts for adiabatic changes due to dynamic changes in Earth's magnetic field. In the following subsections we describe the methodology for calculating ULF wave PSD as well as the methodology to estimate radial diffusion coefficients from the derived PSDs.

2.1 ULF Power Spectral Density

Estimating ULF wave radial diffusion coefficients requires the compressional magnetic field $\boldsymbol{B}_{\parallel}$ and azimuthal electric field $\boldsymbol{E}_{\varphi}$ power spectral density (PSD) (e.g., Fei et al., 2006; Ozeke 2014). To calculate $\boldsymbol{B}_{\parallel}$ and $\boldsymbol{E}_{\varphi}$ we follow the same general framework utilized within the community (e.g., Ali et al., 2015; Ozeke et al. 2014). For each satellite the magnetic and electric fields are rotated into a field aligned coordinate system using a twenty-minute average of the background field to obtain the compressional magnetic field $\boldsymbol{B}_{\parallel}$ and azimuthal electric field $\boldsymbol{E}_{\varphi}$. From $\boldsymbol{B}_{\parallel}$ and $\boldsymbol{E}_{\varphi}$ the PSD can be calculated using several methods such as the multi-taper (Ali et al., 2015; Bentley et al., 2018), wavelet (Dimitrakoudis et al., 2015; Sandhu et al., 2021), or the Fourier transform (Murphy et al. 2011; Rae et al. 2012). In general, each method produces similar estimates of the PSD. Here we use the Fourier transform method outlined in Rae et al. (2012) which has been used in several studies for quantifying ULF wave PSD (Murphy et al. 2011; Murphy et al. 2018) as well as subsequently estimating radial diffusion coefficients (e.g., Ma et al., 2018; Mann et al., 2016; Ozeke et al. 2017; Ozeke et al. 2014). Using this method, the $\boldsymbol{B}_{\parallel}$ and $\boldsymbol{E}_{\varphi}$ PSD is calculated for each satellite from a twenty-minute time window stepped by five minutes. Each PSD is then tagged with the prevailing solar wind and geomagnetic conditions from the OMNI database and the satellites position in L^* corresponding to the middle of the 20-minute window (spectra with no corresponding OMNI or L^* data are dropped from the database).

There are several caveats to note in the calculation of the field aligned coordinates and of the electric and magnetic field PSD. First, the datasets in Table S1 all have different cadences, and so, prior to calculating the PSD, $\boldsymbol{B}_{\parallel}$ and $\boldsymbol{E}_{\varphi}$ are downsampled to 12s so that all time-series have the same cadence. Second, at low L-shells THEMIS and Van Allen Probes rapidly move through L leading to large variations in the background magnetic field. This introduces artificial power into the magnetic field ULF wave PSDs. To circumvent this, for the Van Allen Probes below L = 4 we remove a third-degree polynomial from $\boldsymbol{B}_{\parallel}$; this removes the background magnetic field while aiming to retain the ULF wave fluctuations. Further, we limit Van Allen Probe data to L >3 R_E, whilst for THEMIS data we limit observations to L > 5. Different limits are chosen due to the different rates at which these different satellites cross L along their orbit. Third, both THEMIS and the Van Allen Probes measure with high-fidelity long-wire antennas a two-component electric field in the spin plane; in this study we utilize the Level-2 THEMIS EFI data and Level-3 Van Allen Probes EFW data, both which use the $\boldsymbol{E} \cdot \boldsymbol{B} = 0$ approximation to estimate the third component of the electric field. THEMIS data is further calibrated using SPEDAS (Angelopoulos et al., 2019) while Van Allen Probes Level-3 data has undergone extensive processing by the EFW team (Breneman et al., 2022). Finally, regardless of calibration and data processing it is still possible for poor quality electric and magnetic field data to exist leading to anomalous PSDs. Thus, both the $\boldsymbol{B}_{\parallel}$ and $\boldsymbol{E}_{\varphi}$ PSD spectra are further scrubbed by identifying and removing outliers using the following analysis:

1. Calculate the summed PSD for each of $\boldsymbol{B}_{\parallel}$ and $\boldsymbol{E}_{\varphi}$ spectra between 0.83-15 mHz.
2. Bin the summed PSD datasets by Kp and L-shell.
3. Calculate the interquartile range (IQR) of each bin (upper quartile-lower quartile, Q_U-Q_L)
4. Identify outlying spectra as any spectra whose summed PSD is less than Q_L-1.5*IQR or greater than Q_U+1.5*IQR and are removed from the PSD data set.

This method of scrubbing data and removing outliers is often used in statistical analysis and data sciences. In our study, this method does an excellent job removing anomalously high power associated with erroneous or unphysical data. For example, prior to removing outliers the mean spectrum is larger than the upper quartile spectra. Once the outliers are removed, the mean spectrum closely follows the upper quartile spectrum; though this still represents a skewed distribution, the similarity between the mean and upper quartile is in agreement with previous statistical studies of ULF wave PSD (e.g., Bentley et al., 2018; Murphy et al. 2011).

Once processed, scrubbed, and tagged with the OMNI data and L^* position there are over 1.7 million magnetic and 0.46 million electric field PSD which span nearly an entire solar cycle and cover the entire inner magnetosphere through a variety of solar wind and geomagnetic conditions. Figure 1 shows the median $\boldsymbol{B}_{\parallel}$ (top) and $\boldsymbol{E}_{\varphi}$(bottom) PSD at each frequency (y-axis) as function of Kp (x-axis) and L^* (panels 1-8). Evident in Figure 1 is that power is concentrated at lower frequencies and increases at all frequencies with Kp, consistent with previous studies (Ali et al., 2015; Brautigam & Albert, 2000; Rae et al. 2012). Panels 9 of Figure 1 (far right) shows how the PSD varies with L^* and Kp at a fixed frequency of 2.5 mHz. Consistent with previous studies this final panel demonstrates that ULF wave PSD increases with both L^* and geomagnetic activity as parameterized by Kp. The database of PSD spectra described and shown in Figure 1 is used to estimate D_{LL}^{E} and D_{LL}^{B} as described in the next subsection.

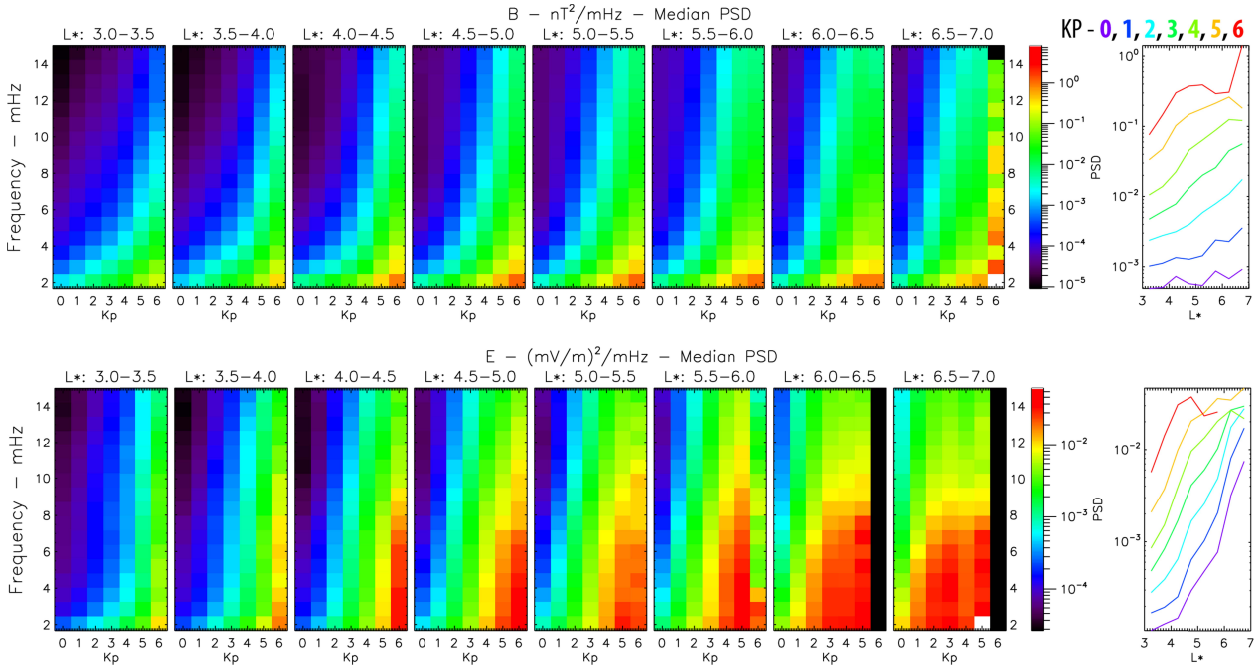

Figure 1: Statistical variation of the $\boldsymbol{B}_{\parallel}$ (top) and $\boldsymbol{E}_{\varphi}$(bottom) PSD. The spectral plots show the median PSD as a function of frequency (y-axis), Kp (x-axis) and L^* (panels 1-8). The line plots show the variation of PSD at fixed a frequency of 2.5 mHz as a function of L^* and Kp (color) for the entire dataset.

2.2 Radial Diffusion Estimation

Radial diffusion coefficients can be calculated in several ways (e.g., Fei et al., 2006; Schulz & Lanzerotti, 1974). In this work, since we are utilizing $\boldsymbol{B}_{\parallel}$ and $\boldsymbol{E}_{\varphi}$ we use the framework outlined by Ozeke et al. (2014) and Mann et al. (2016) which follows the Brizard and Chan (2001) and Fei et al. (2006) formalism.

Ozeke et al. (2014) developed expressions for the electric and magnetic radial diffusion coefficients which depend on the azimuthal electric field and compressional magnetic field PSD and which are energy and azimuthal wave number independent (see equations 19 and 22). In their work Ozeke et al. (2014) used in-situ THEMIS and GOES observations to quantify the compressional magnetic field $\boldsymbol{B}_{\parallel}$ PSD and ground-based magnetometer observations to quantify the azimuthal electric field $\boldsymbol{E}_{\varphi}$ PSD. The

statistical variation of these PSD as a function of Kp were substituted into equations 19 and 22 to derive analytical Kp dependent function of D_{LL}^{B} and D_{LL}^{E}.

In a follow on study, Mann et al. (2016) expanded on the Ozeke et al. (2014) framework to derive event-specific D_{LL}^{E}s from ground-based magnetometers. Mann et al. (2016) averaged the ULF wave PSD over a fixed frequency range and substituted it into equation 22 of Ozeke et al. (2014) to derive time-dependent-event-specific diffusion coefficients. In their study Mann et al. (2016) used these event specific diffusion coefficients to model the formation of the outer and storage radiation belts observed by the Van Allen Probes in September 2012 (Baker et al. 2013). These authors demonstrated that event-specific ULF wave radial diffusion coefficients coupled with dynamic boundary conditions reproduced the double belt structure of the outer radiation belt, highlighting the importance of ULF wave radial diffusion in controlling the dynamic topology of the outer radiation belt. Several follow-on studies have used the same methodology as Mann et al. (2016) to derive event-specific ULF wave radial diffusion coefficients to study the importance of radial diffusion radiation belt dynamics. In general, these studies have demonstrated that radiation belt simulations using event specific radial diffusion coefficients perform better, in that they more accurately reproduce radiation belt electron dynamics, than those that do not (Ma et al., 2018; L. G. Ozeke et al., 2019, 2020).

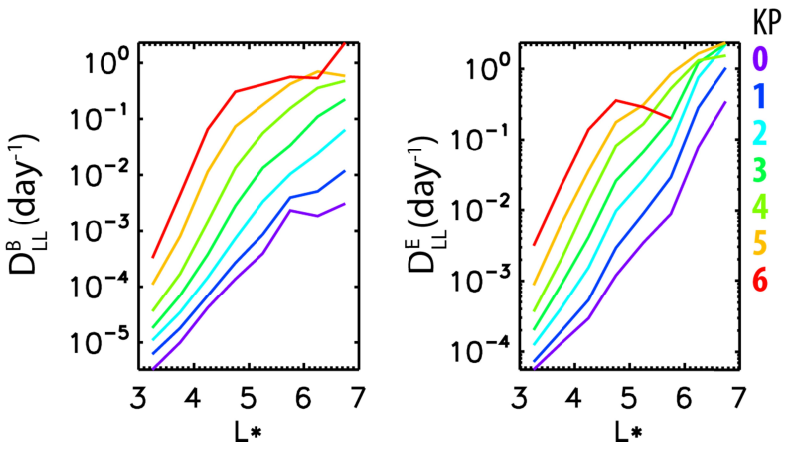

Figure 2: Median D_{LL}^{B} (left) and D_{LL}^{E}(right) as function of L^{*} and Kp for the entire dataset.

Here, we use the same approach as Mann et al. (2016) to derive in-situ D_{LL}^{E} and D_{LL}^{B} from the $\boldsymbol{E}_{\varphi}$ and $\boldsymbol{B}_{\parallel}$ PSD using equations 19 and 22 from Ozeke et al. (2014). Each spectrum from the PSD database is averaged between 0.83-15.00 mHz. The averaged $\boldsymbol{B}_{\parallel}$ and $\boldsymbol{E}_{\varphi}$ PSD are then substituted into equations 19 and 22 of Ozeke et al. (2014) providing an energy and azimuthal wave number independent estimate of D_{LL}^{B} and D_{LL}^{E} respectively. Figure 2 shows the median D_{LL}^{B} (left) and D_{LL}^{E}(right) as a function of L^{*} and Kp. The D_{LL}s are similar in magnitude to other studies and increase with L^{*} and increasing geomagnetic activity (e.g., Ozeke et al. 2014). At higher Kp values (e.g., 5 and 6), the magnitude of D_{LL}^{B} is comparable to D_{LL}^{E}. This is consistent with recent work that has demonstrated that during the main phase of storms the magnitude of D_{LL}^{B} ~ D_{LL}^{E} (Olifer et al., 2019; Sandhu et al., 2021). It is important to note that in this approach $\boldsymbol{E}_{\varphi}$ and $\boldsymbol{B}_{\parallel}$ are treated independently whereas in fact they fact they are correlated via Faraday's law. In addition, the electric field includes both the electrostatic as well as the

electromagnetic component. Regardless, recent work has demonstrated that the resulting diffusion coefficients are within a factor of approximately two of the electromagnetic diffusion coefficients (Lejosne, 2019). In the next section we describe the development of a radial diffusion model utilizing the database of D_{LL}s described here.

3 Radial Diffusion Model

ULF wave radial diffusion is a key component of radiation belt dynamics, driving periods of enhanced electron loss via outward radial transport as well as electron acceleration via inward transport (e.g., Ozeke et al. 2017). In radiation belt models, the strength of ULF wave radial diffusion is specified by diffusion coefficients D_{LL} (e.g., Brizard & Chan, 2001; Fei et al., 2006). Several researchers have developed models which specify the strength of radial diffusion coefficients as a function of geomagnetic activity from both in-situ and ground-based observations of ULF wave PSD (Ali et al., 2015; Brautigam & Albert, 2000; Ozeke et al. 2014). In this section we build on these studies using a database of satellited-derived ULF wave D_{LL}^{E} and D_{LL}^{B} radial diffusion coefficients in an attempt to develop a more robust characterization of the rates of ULF wave radial diffusion based on known drivers of ULF waves. Here we describe the development of the radial diffusion model including a parametric study to identify a robust set of independent variables as model inputs, a discussion of different model types/algorithms, and training, testing, and performance of a final model. In section 4 we investigate the final model, including its performance under different geomagnetic conditions (e.g., quiet and storm times) and comparing to existing diffusion models.

3.1 Parametric Study

Previous studies developing radial diffusion models parameterized their diffusion coefficients based on the planetary index Kp. Kp is a three-hour index ranging from 0 to 9; the indices correspond to exponentially increasing perturbations of Earth's magnetic field as characterized by several ground-based magnetometers from around the world. While Kp is a good measure of geomagnetic activity, its utility in models is limited for three reasons. First, Kp is a measure of the response of the coupled solar wind-magnetosphere-ionosphere system as opposed to a driver of the dynamics of this system. Second, the three-hour cadence is long compared to storm-time radiation belt time-scales (Olifer et al., 2018; Ozeke et al. 2017). Finally, the exponentially increasing index limits the dynamic range of models, requiring models to extrapolate to high values of Kp during very active times. For example, the Brautigam and Albert (2000) and Ozeke et al. (2014) models are limited to using data derived for conditions with Kp≤6 while Liu et al. (2016) and Ali et al. (2016) diffusion models are limited to a maximum Kp value of 5. Above these values the respective models must extrapolate to higher Kp values to estimate the magnitude of radial diffusion coefficients under active conditions. Despite these limitations, there is a key advantage in that the D_{LL}s parameterized by Kp in that they can be easily forecasted when forecasts of Kp are readily available (Glauert et al., 2021; Horne et al. 2021).

In this work we use the OMNI dataset to parameterize and develop models of radial diffusion at higher cadence using known drivers of ULF waves. The OMNI data has a higher cadence (1 hour, 5 minute, and 1 minute) than the Kp index. This is ideal for radiation belt models as it provides increased temporal dynamics and resolution. In addition, the OMNI dataset contains multiple parameters including the solar wind vector magnetic field, dynamic pressure, the vector solar wind velocity, as well as multiple

geomagnetic indices. This allows for the development of models with multiple inputs which can increase model performance; however, one must identify an ideal set of inputs which maximizes model performance, while maintaining model stability (e.g., modelled D_{LL}s do not exhibit high variance with certain combinations of variables) and simplicity (e.g., avoiding the addition of variables with little impact).

In our development of new parameterizations of D_{LL}^{B} and D_{LL}^{E} we perform a parametric study of L^* a proxy of the third adiabatic invariant, $Sym\text{-}H$, the GSM y and z components of the interplanetary magnetic field (IMF; B_y and B_z), solar wind speed V and x-component V_x GSM, and the solar wind dynamic pressure (P_{dyn}) and density (n) to identify the best combination of independent variables (or inputs) with which to develop models of D_{LL}^{B} and D_{LL}^{E}. From this set of independent variables, L^* is the only required variable in our model as it defines the radial diffusion coefficients on a set grid as is required for its implementation in radiation belt simulations. Unlike other models we use L^* as it is more physically meaningful then radial distance or L as it accounts for adiabatic changes due to the dynamic magnetic field. The other independent variables selected for our parametric study correspond to known drivers of ULF wave power in the magnetosphere (Bentley et al., 2018; Kepko et al., 2002; Mathie & Mann, 2001; Murphy et al. 2015; Rae et al. 2019).

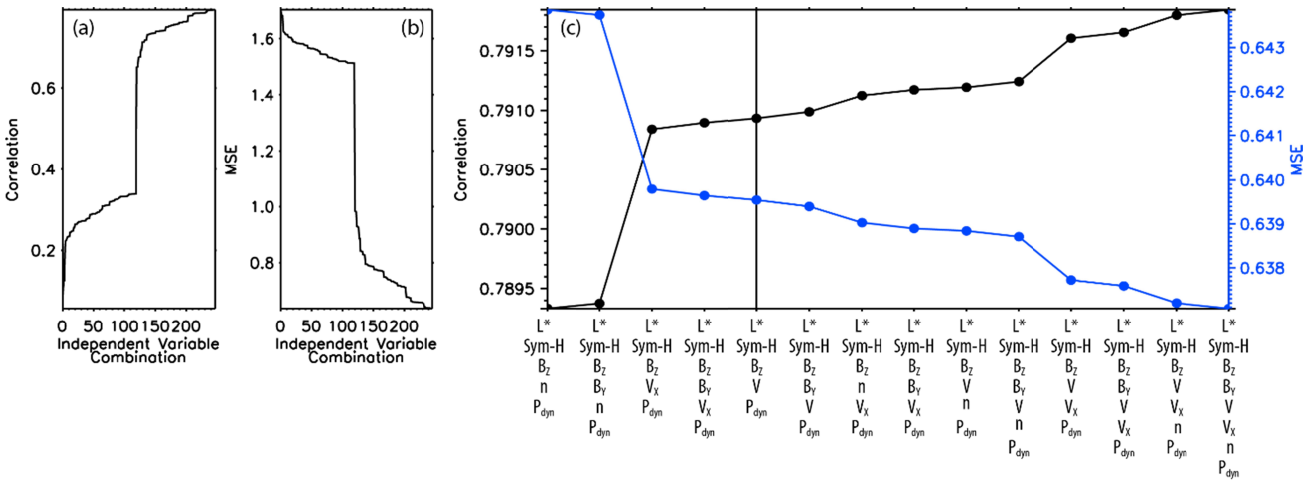

Figure 3: Results of the parametric study. (a) and (b) Correlation and mean square error (MSE) of data and multi-linear regression model for all combinations of independent variables (identified as integers on the x-axis). (c) A zoom in of (a) and (b) highlighting the combination of independent variables resulting in a high correlation and low MSE between the data and multi-linear regression model; the black line is the correlation and blue the MSE, the x-axis shows the various combinations of independent variables.

To identify an optimized set of independent variables the parametric study loops through every combination of input variables and fits a multi-linear regression model to the $\log_{10}$ of D_{LL}^{B}. For each model we determine the model-data correlation and mean square error (MSE). Using the correlation and MSE we identify the best combination of independent variables to subsequently train final models of D_{LL}^{B} and D_{LL}^{E}. Figure 3 shows the results of this parametric study; panels a and b show the correlation and MSE for every combination of variables (identified simply as integers on the x-axis). Evident in panels a and b is that the correlation increases and MSE decreases for different combinations of inputs.

Figure 3c focuses on the combination of variables which maximize the correlation and minimize the MSE of the trained model. Evident in Figure 3c is that combinations of L^*, $Sym\text{-}H$, IMF B_z and P_{dyn} coupled with various combinations of IMF B_y, V, V_x, and n all lead to high correlations and low MSE. The correlation peaks and MSE minimizes when all input variables are used in the parametric study; however, this introduces significant multicollinearity between the input variables (e.g., B_z and B_y, V and V_x) which can decrease model performance as well as adding additional complexity. From the parametric study, L^*, $Sym\text{-}H$, B_z, V, and P_{dyn}, are identified as an optimized set of input parameters to model D_{LL}^B (vertical line Figure 3c); the correlation is high, MSE low, and the correlation between input variables is limited compared to the other combination of inputs while also maintaining a level of simplicity by including only five independent variables. A similar dependence has also been discussed by Dimitrakoudis et al. (2022), albeit for ULF wave power which is directly related strength of radial diffusion. Finally note, that the correlations and MSE for this set of independent variables is on the same order as those when Kp and L^* are considered as independent variables. However, in this paper we focus on developing a model based on known drivers of ULF wave power as opposed to variables and indices which respond to ULF wave power and enhanced geomagnetic activity like Kp. Thus, for the purpose of this study the combination of L^*, $Sym\text{-}H$, IMF B_z, V, and P_{dyn} are used as independent variables train models of D_{LL}^B and D_{LL}^E.

3.2 D_{LL} Model

There are several methods and algorithms which could be used to generate or train models for the parameterization of the electric and magnetic field D_{LL}s. In this work we investigated two algorithms for training models of D_{LL}^B and D_{LL}^E, a multi-linear regression model (Murphy et al. 2015, 2020), and a neural network model (Bortnik et al., 2018). In general, both the multi-linear regression and neural network models performed similarly using the independent variables identified in Section 3.1; both algorithms produced similar correlations and MSEs when fitted to D_{LL}^B and D_{LL}^E. Given the similar model performance, we use a multi-linear regression model for the final parameterisation we present here due to its simplicity as compared to the implementation, use, and sharing of neural networks.

In developing the multi-linear regression models, the D_{LL}^B and D_{LL}^E datasets are first regularized as a function of L^*. The regularization ensures that the distribution of D_{LL}s as a function of L^* is uniform, i.e., the number of D_{LL} data points for any given L^* is the same. This is important as the spacecraft spend more time at apogee, high L^*, which can bias any model by fitting to the bulk of the data which are preferentially located in one part of the domain. The datasets are then randomly separated into train/test sets using a 70/30 percent split. The models are trained on the train set while the test set is used to verify performance. Before training, the independent variables are normalized between 0 and 1 by the maximum and minimum values in the train set; this normalization ensures the dependence on each of the independent variables is assessed on a similar scale and generally increases the stability and performance of the resulting models. Finally, we restrict the model space to $L^* \in [3,7]$; this encompasses the outer radiation belt and in general improves model performance by removing highly variable data at higher L^*. Though this limits the dynamic range of the data used to train the linear regression models, the linear regression models can still be used calculate D_{LL}s outside this range. However, care must be taken when extending the model outside these limits as it is not possible to test

the models performance in these regions. This final dataset is then fitted to the $\log_{10}$ of D_{LL}^{B} and D_{LL}^{E} following the functional form shown in Equation 1; the D_{LL}s can then be calculated as shown in Equation 2.

$$log_{10}(D_{LL}) = c + a_1 L^* + a_2 Sym\text{-}H + a_3 B_z + a_4 V + a_5 P_{dyn} \quad (1)$$

$$D_{LL} = 10^{c + a_1 L^* + a_2 SymH + a_3 B_z + a_4 V_t + a_5 P_{dyn}} \quad (2)$$

Figure 4 shows the results of the training of the linear models for D_{LL}^{B} and D_{LL}^{E}. The left column of Figure 4 shows the residuals, defined as the difference between the model and satellite-derived $\log_{10} D_{LL}$ (referred to as the residuals), for both the train and test datasets (red and blue) and both D_{LL}^{B} and D_{LL}^{E} (top and bottom). For both D_{LL}^{B} and D_{LL}^{E} the residuals are normally distributed and peak around zero for both test and train data sets (left column). This is ideal as it demonstrates that in general the modelled D_{LL}s are similar to the satellite-derived D_{LL}s. Further, the similarity in the distributions of train and test residuals indicates that the model does not suffer from overfitting (e.g., fitting only to the training data).

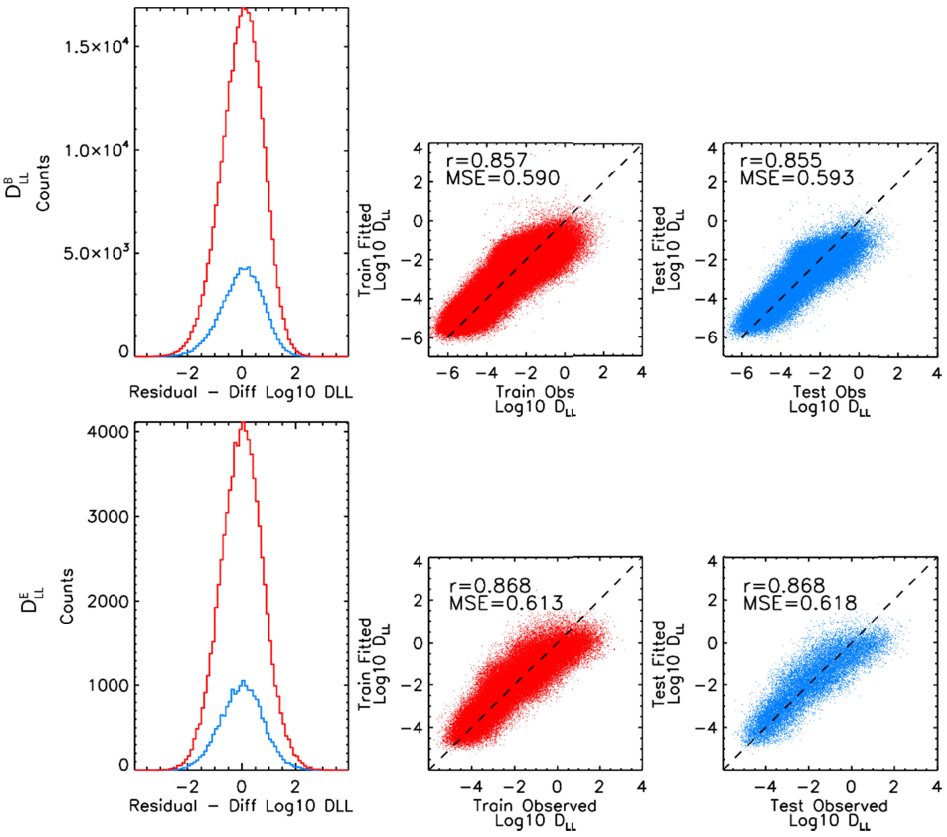

Figure 4: The residuals for the multi-linear regression D_{LL}^{B} and D_{LL}^{E} models (top and bottom). Right, distribution of the residuals for the train and test data sets (red and blue). Middle and right, observed D_{LL} versus modelled D_{LL} for the train and test data sets (blue and red); in each panel the correlation, r, and MSE are shown in the top left.

The middle and right columns of Figure 4 show the observed D_{LL} versus the modelled D_{LL} for both the train and test datasets (middle and right); the correlation and MSE are shown in the top left. For both D_{LL}^{B} and D_{LL}^{E} the correlation between the modelled and observed D_{LL}s in both the train and test data

sets is high, ~0.86 accounting for ~74% of the variance within the data sets. For both models the MSE is also low. Overall, the normal distribution of the residuals, high correlation and low MSE, coupled with the similarities between the train and test data sets demonstrates the robustness and accuracy of the trained models. Table S2, shows the fitting and normalization coefficients for both D_{LL} models as described by Equations 1 and 2.

3.3 Model Performance

In this section we investigate the residuals as a function of each independent variable to provide the reader and specifically modelers with a clear overview of the model's performance under varying conditions. Figure 5 shows the probability distribution functions (PDFs) of the D_{LL}^{B} and D_{LL}^{E} model residuals (top and bottom; modelled D_{LL} minus satellite-derived D_{LL}) as a function of the independent variables (rows) for the combined train and test datasets. In general, both the D_{LL}^{B} and D_{LL}^{E} models perform well as a function of the independent variables. The residuals are peaked around zero as a function of the independent variable. However, this is not true for L^* and for more extreme values of $Sym\text{-}H$, B_z, and P_{dyn}. With regard to L^*, both the D_{LL}^{B} and D_{LL}^{E} models show bias at $L^* > 6$ and $L^* < 4.5$ where the residuals are skewed to either positive or negative values. The biases in L^* are more pronounced than those observed as a function of $Sym\text{-}H$, B_z, and P_{dyn} and are likely the result of biases that exist in in the calculation of L^*. Note, a similar distribution of residuals is observed when considering only storm-time or quiet-time periods with this choice of independent variables. This similarity is ideal as it demonstrates that both the D_{LL}^{B} and D_{LL}^{E} radial diffusion models perform well during both storm- and quiet-times. This was not the case for storm- and non-storm-time Kp-parameterisation of D_{LL} examined by Dimitrakoudis (2022) which highlights another pitfall of parametrizing D_{LL} by Kp as such parameterizations cannot account for both storm and quiet times. Due to the similarity between storm-time, quiet-time, and all data, the storm- and quiet-time distributions are shown in Supporting Information S3 and S4.

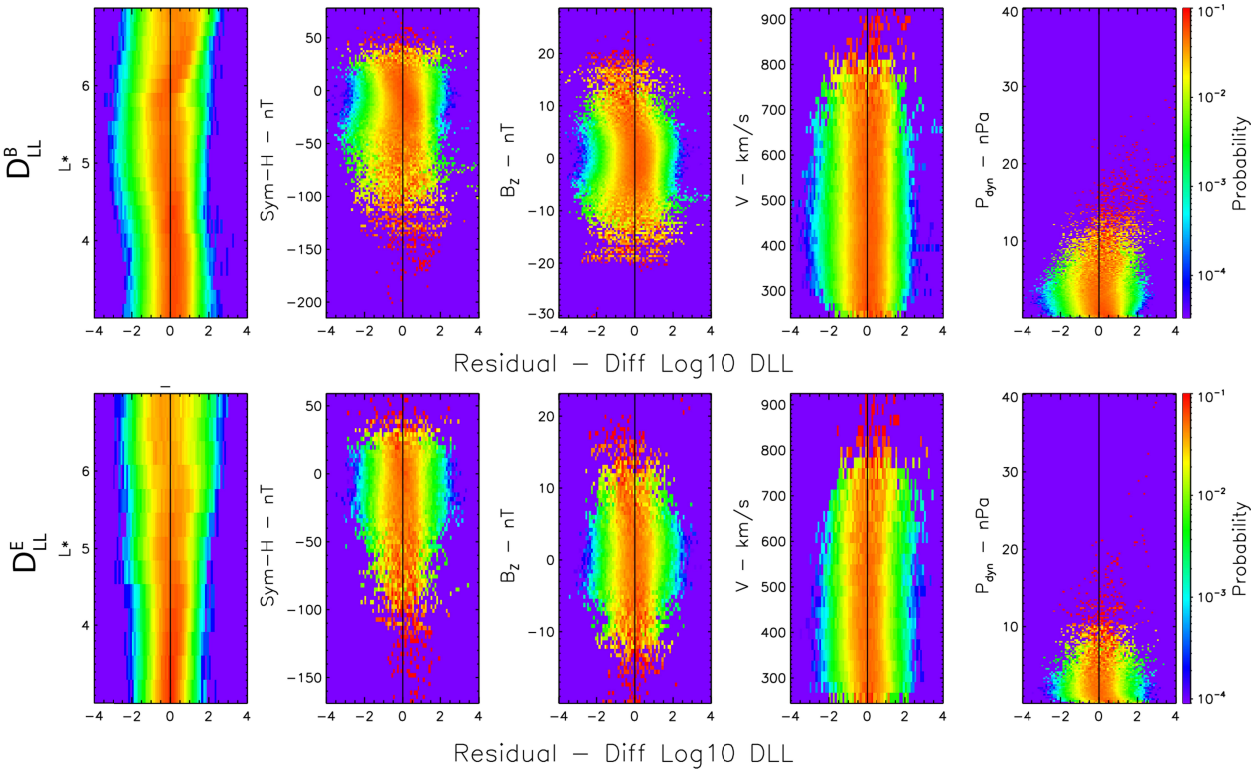

Figure 5: PDFs of the D_{LL}^{B} and D_{LL}^{E} model residuals calculated from the combined train and test data sets for each of the independent variables.

While the overall performance of both the D_{LL}^{B} and D_{LL}^{E} diffusion model is good (Figure 4) the biases as a function of L^* may introduce errors which can propagate through any radiation belt simulation. For this reason, the residuals have been characterized as a function of L^* so that the bias can be readily removed from the models. To remove the bias, we use the residual-L^* PDF. The data is binned in L^* in increments of 0.1 (corresponding to the grid size in many radiation belt simulations) and so are the residuals. For each L^* bin we fit a Gaussian of the form shown in equation 3, where A_0 is the height, A_1 is the center, and A_2 is the width (standard deviation) of the fitted Gaussian. This analysis is shown in Supporting Information Figure S5 for both the D_{LL}^{B} and D_{LL}^{E} models and several select L^* bins. From these fits we can use $A_1$to shift the modelled D_{LL}s by subtracting A_1 from the modelled D_{LL} corresponding to a particular L^* bin. In this way when the residuals are recalculated they peak around zero.

$$f(r) = A_0 e^{(\frac{r-A_1}{A_2})^2} \quad (3)$$

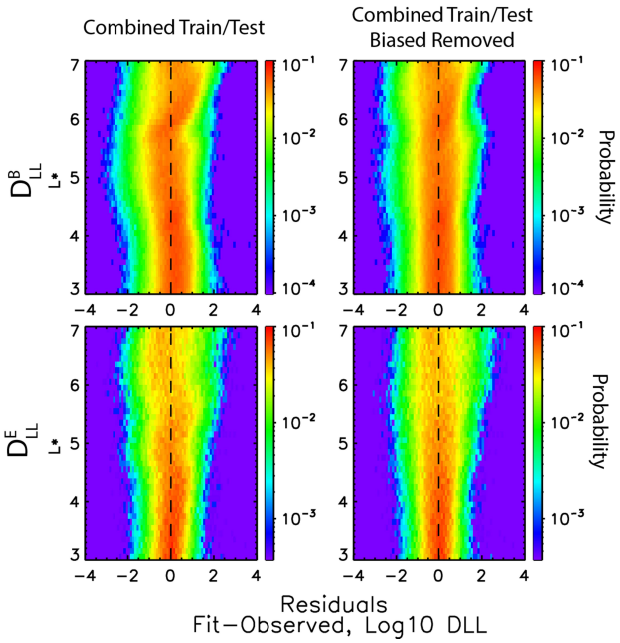

Figure 6: Comparison of the PDFs of both D_{LL}^{B} (top) and D_{LL}^{E} (bottom) model residuals (left) and residuals-biased-removed (right) of the combined train/test datasets

Figure 6 shows the results of the biased-removed D_{LL}s calculated by shifting each D_{LL} based on the Gaussian fits and corresponding L^* bin. The left column shows the PDF of residuals versus L^* and the right column shows the PDF of the residuals-biased-removed versus L^* for the combined trained/test datasets. Evident in Figure 6 is that once the bias is removed from the modelled D_{LL}s the residuals peak around zero and the bias as a function of L^* is no longer evident. In this analysis it is important to note that bias as function of L^* is discrete and not continuous; however, the bias has been characterized on an L^* grid typically used in radiation belt simulations. Finally, though not the purpose of characterizing residuals, the Gaussian fits provide a very simple means to generate ensembles of D_{LL}s which can be used in radiation belt simulations. For example, the width and center of the Gaussian can be used with a random number generator to sample from the fitted distribution of residuals and subtract the randomly sampled residual from the modeled D_{LL}s. In this way several D_{LL} time series can be generated to run ensemble simulations of the radiation belt response. Supporting Information Table S6 contains the Gaussian fit parameters as a function of L^* for both D_{LL}^{B} and D_{LL}^{E}. Note that the shift in the residuals, defined by the center of the Gaussian is largest for D_{LL}^{B} and that the D_{LL}^{E} model performs better then the D_{LL}^{B}. Finally, while these corrections help with the model residuals, they are generally small, not exceeding a factor of ~2.

4 Event Case studies and Model Comparisons

In the previous section we discussed the development of new D_{LL}^{B} and D_{LL}^{E} models and assessed their overall performance as a function of each independent variable. In this section we investigate the dynamics and performance of the new D_{LL}^{B} and D_{LL}^{E} models during two case studies, an extended period of quiet geomagnetic activity and the March 2013 Geospace Environment Modeling Quantitative Assessment of Radiation Belt Modeling focus group storm challenge event (e.g., Engebretson et al., 2018; Ma et al., 2018). For both cases we compare the D_{LL}s derived here with the Ozeke et al. (2014),

Brautigam and Albert (2000), and Lejosne (2019) D_{LL}s. Note the Ozeke et al. (2014), Brautigam and Albert (2000), and Lejosne (2019) D_{LL}s are all parameterized by L and not L^*; however, since such models are routinely used in simulations with no conversion to L^* we are able to compare them to the model developed here assuming their L is directly used as L^* in simulations.

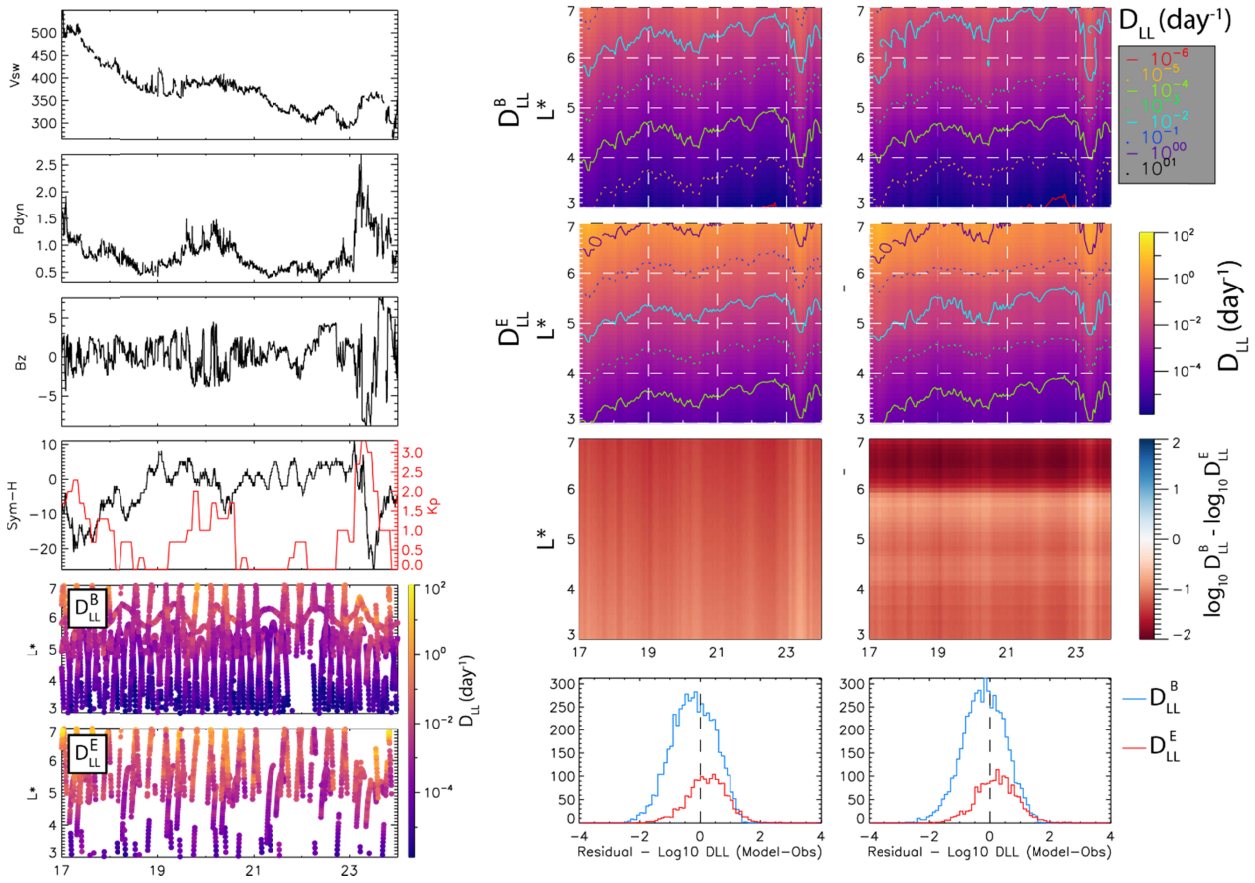

Figure 7: The modelled D_{LL}s during an interval of quiet solar wind and low geomagnetic activity. From top to bottom the left panel shows V, P_{dyn}, B_z, $Sym\text{-}H$ (black) and Kp (red), and the satellite derived D_{LL}^B and D_{LL}^E. The middle and right panel show the modelled and model-bias-removed D_{LL}s. From top to bottom the two right panels show D_{LL}^B, D_{LL}^E, the difference between the log of D_{LL}^B and D_{LL}^E, and then the model residuals calculated by comparing the modelled D_{LL}s to the satellite derived D_{LL}s. The contours in the top two panels are contours of constant D_{LL}, the white dashed lines are placed at major tick marks to aid in comparison between the model and model-bias-removed D_{LL}s.

Figure 7 provides an overview of the solar wind and geomagnetic conditions as well as the satellite-derived D_{LL}s during a quiet solar wind and geomagnetic period in November 2013 (see caption for details). At the start of the quiet period the solar wind speed was elevated and $Sym\text{-}H$ slightly negative for ~12 hours. Towards the end of the interval the IMF turned southward in association with a period of enhanced dynamic pressure and another period of negative $Sym\text{-}H$ lasting ~24 hours. Throughout the quiet interval Kp remained low, below 3+. The observed D_{LL}s were largest at the start and end of the quiet period, in association with elevated solar wind speeds and enhanced dynamic pressure and southward IMF. Through the middle of the quiet period the observed D_{LL}s were generally small. This can be seen in the bottom two rows of the left panel. Throughout the quiet period the modelled D_{LL}s

(middle and right panels) showed the same overall pattern as the observed D_{LL}s and the modelled residuals remained consistent with the overall model performance (bottom panels of middle and right column). There is also little difference between the modeled D_{LL}s and the modeled-biased-removed D_{LL}s through the duration of the quiet period. Finally, in both models D_{LL}^{E} is larger then D_{LL}^{B} by about an order of magnitude; this is generally consistent with the difference between D_{LL}^{E} and D_{LL}^{B} for higher energy electrons in Ozeke et al. (2014).

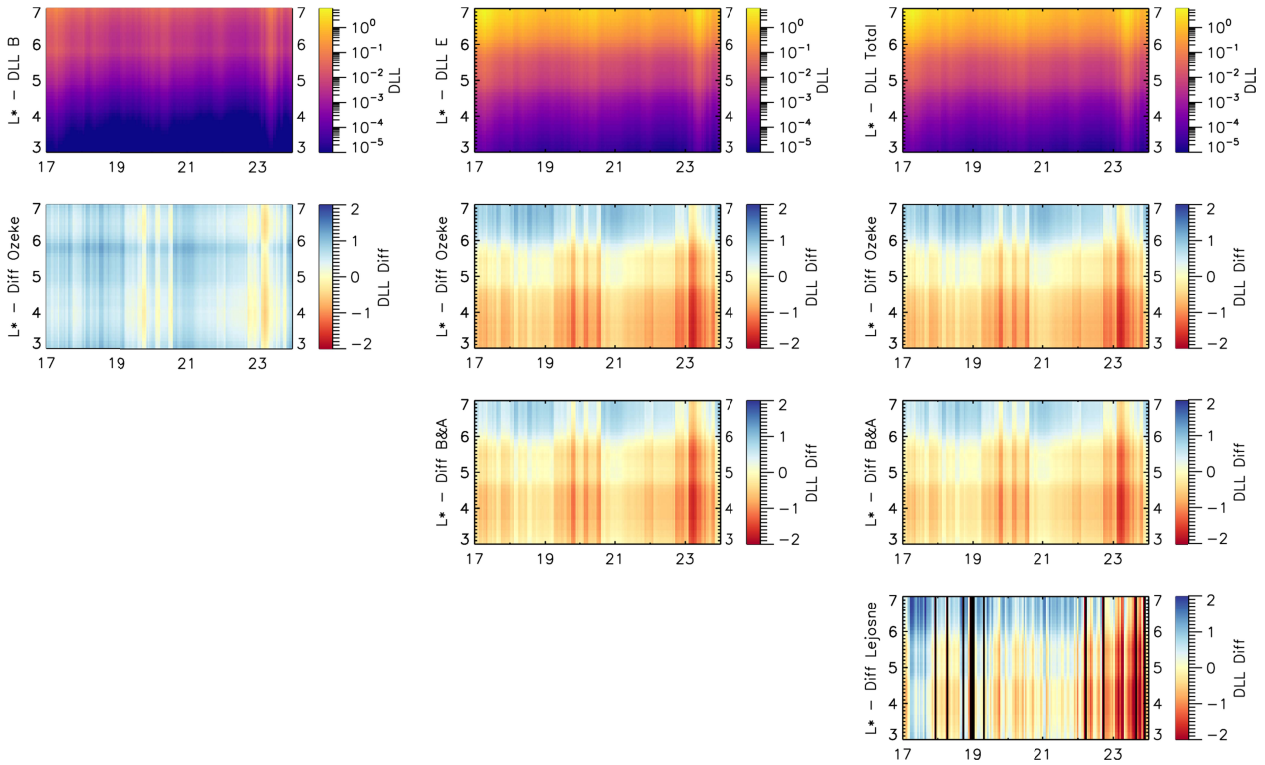

Figure 8: A comparison of bias-removed D_{LL}s derived here and those from Ozeke et al. (2014), Brautigam and Albert (2000), and Lejosne (2019). From left to right the columns show D_{LL}^{B}, D_{LL}^{E}, and $D_{LL}^{T} = D_{LL}^{B} + D_{LL}^{E}$. From top to bottom the rows show the modelled D_{LL}s derived here followed by the difference between the logs of modelled D_{LL}s and those from Ozeke et al. (2014), Brautigam and Albert (2000), and Lejosne (2019).

During the quiet interval the modelled D_{LL}s vary as one would expect. They were highest during elevated solar wind speed and negative $Sym\text{-}H$, and again with southward IMF, increased P_{dyn}, and negative $Sym\text{-}H$. However, what is more interesting, is the comparison between the D_{LL}s derived here and existing models of D_{LL}s (Figure 8). The top row of Figure 8 shows the modelled D_{LL}^{B}, D_{LL}^{E}, and the total $D_{LL}^{T} = D_{LL}^{B} + D_{LL}^{E}$, with the biases-removed. The subsequent rows show the difference between the logs of the model bias-removed D_{LL}s and the Ozeke et al. (2014), Brautigam and Albert (2000), and Lejosne (2019) $D_{LL}s$ (see Figure caption for additional details). Compared to Ozeke et al. (2014), the modeled D_{LL}^{B} derived here is larger while the modeled D_{LL}^{E} derived here is larger at higher L^* and smaller at lower L^*. The combined diffusion D_{LL}^{T} shows the same pattern as D_{LL}^{E}. For Brautigam and Albert (2000) we only consider their electromagnetic term as the electrostatic term is typically ignored in radiation belt simulations (Ozeke et al. 2013). In this case the electromagnetic diffusion is larger than D_{LL}^{E} at higher L^* and smaller at lower L^*; the modelled D_{LL}^{T} shows the same pattern when compared to

the Brautigam and Albert (2000) electromagnetic term. A similar pattern is also observed when comparing with the Lejosne (2019) D_{LL}s. In this case we only compare D_{LL}^{T} to those of Lejosne (2019) as there is no analogous D_{LL}^{E} or D_{LL}^{B}. Note the Brautigam and Albert (2000) electromagnetic term and Ozeke et al. (2014) D_{LL}^{E} are very similar in magnitude.

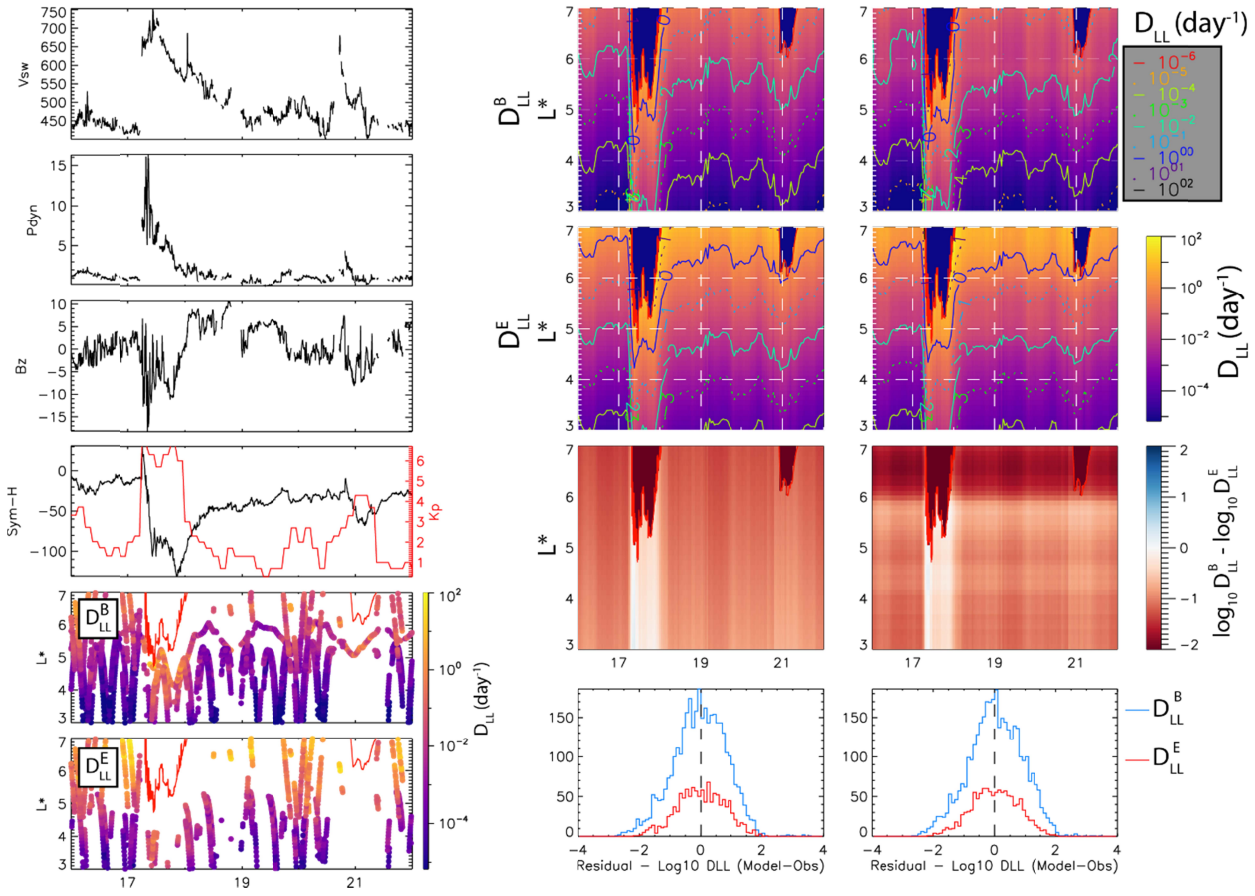

Figure 9: Solar wind dynamics, geomagnetic activity, satellite derived D_{LL}s, and modelled D_{LL}s during a geomagnetic storm in March 2013. The figure is in the same format as Figure 7. The red traces in the bottom two panels of the left column and top two panels of the middle and right column show the position of the last close drift shell throughout the interval.

Figure 9 and Figure 10 show the same set of observations, model-data comparison, and model-model comparison as Figure 7 and Figure 8 for the March 2013 storm. The storm is associated with high-speed solar wind, and ~1 day of large dynamic pressure and southward IMF (left panel Figure 9). This leads to a large geomagnetic storm where the last closed drift shell reaches below geosynchronous orbit (red trace in Figure 9 and Figure 10), Kp exceeds 6, and $Sym\text{-}H$ reaches nearly -150 nT. During the main phase of the storm, March 17, D_{LL}^{B} peaks and even exceeds D_{LL}^{E} during the same interval. This is consistent with other studies which have shown D_{LL}^{B} to be large during the main phase of storms (Olifer et al., 2019; Sandhu et al., 2021). Following the main phase and through the recovery phase both D_{LL}^{B} and D_{LL}^{E} decay reaching pre-storm levels before rapidly enhancing again on March 21 during a second interval of fast solar speed and southward IMF. These patterns are seen in the satellite-derived, modelled, and modelled-biased-removed D_{LL}s (left, right and middle panels) and are consistent with what would be

expected given the solar wind and geomagnetic activity. Comparing the modelled and modelled-bias-removed D_{LL}s there is generally little difference. The model bias-removed D_{LL}^{B} is slightly smaller at high and low L^*. During the main phase $D_{LL}^{B} \approx D_{LL}^{E}$ in both models. Finally, the residuals for both models are normally distributed and peak around zero.

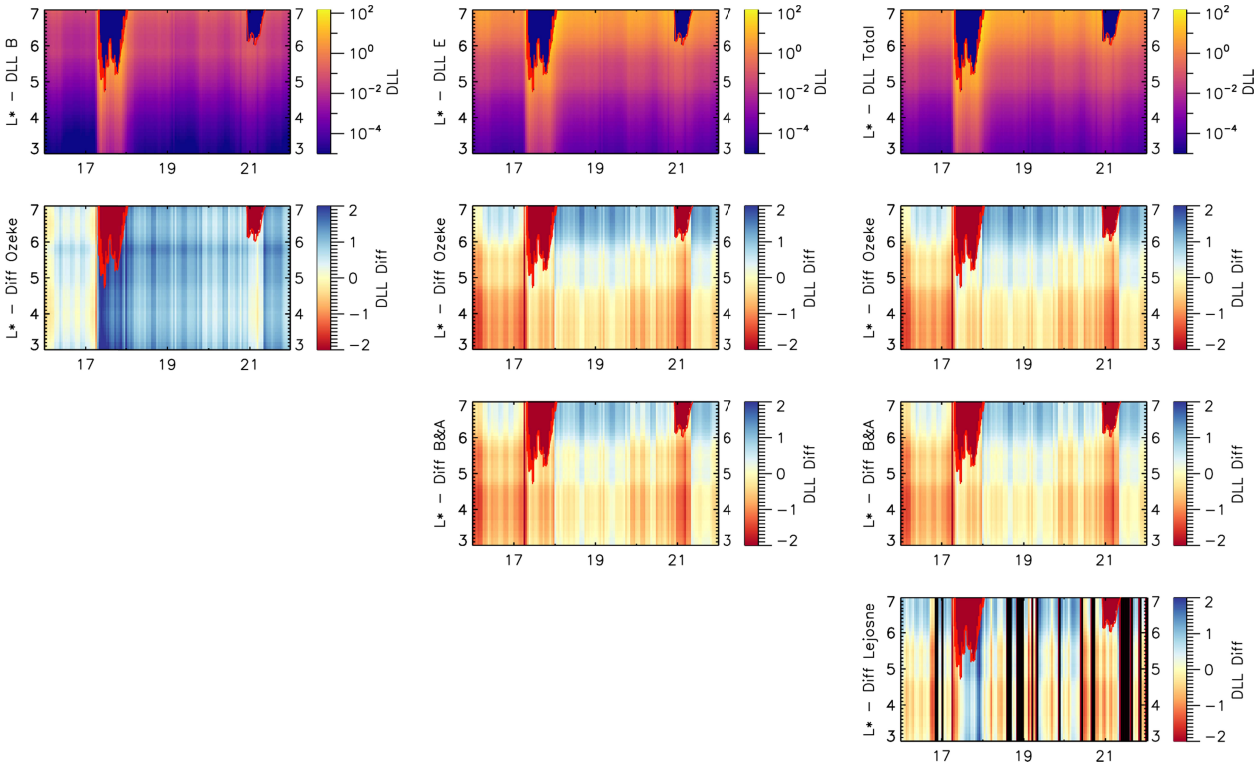

Figure 10: A comparison of the bias-removed D_{LL}s derived here and those from Ozeke et al. (2014), Brautigam and Albert (2000), and Lejosne (2019) during a geomagnetic storm in March 2013. The figure is in the same format as Figure 8. The red lines show the position of the last close drift shell throughout the interval.

During the geomagnetic storm (Figure 10) the D_{LL}s derived here show a similar relation to the Ozeke et al. (2014), Brautigam and Albert (2000), and Lejosne (2019) D_{LL}s as that observed during quiet times (Figure 8). $D_{LL}^{B}$is larger than that of Ozeke et al. (2014), especially during the main phase of the storm (Figure 10 left). At high L^*, D_{LL}^{E} is larger than that of Ozeke et al. (2014) and Brautigam and Albert (2000) and smaller at low L^* (Figure 10 Figure 10 middle). Comparing D_{LL} total (column 3) the D_{LL}s derived here are larger at higher L^* and smaller at lower L^* as compared to Ozeke et al. (2014) and Brautigam and Albert (2000) (Figure 10 right). Compared to Lejosne (2019) the D_{LL}s derived here are larger during the main phase of the storm and at higher L and are generally smaller at lower L^* (Figure 10 bottom right). Prior to the storm main phase, March 16, D_{LL}^{E} and D_{LL} total derived here are smaller then the other three models across all L^*. During this period Kp is elevated compared to quiet values reaching a Kp of 4, while the solar wind remains quiet accounting for the differences between the models.

5 Summary and Conclusions

In this work we utilize in-situ observations to develop a database of ULF wave power spectral density (PSD) and satellite-derived ULF wave radial diffusion coefficients, D_{LL}s. The database of satellite-derived

D_{LL}s is used to construct a new L^* dependent and optimized bias-removed model of D_{LL}^B and D_{LL}^E driven by B_z, V_{sw}, P_{dyn} and $Sym\text{-}H$. Overall, the new models of D_{LL}^B and D_{LL}^E perform well when compared to the satellite-derived D_{LL}s from which the models were developed.

The new bias-removed D_{LL}s derived where compared to existing D_{LL} models from Ozeke et al. (2014), Brautigam and Albert (2000), and Lejosne (2019) during a period of quiet geomagnetic activity and the March 2013 geomagnetic storm. If one ignores the main phase of the storm, the comparison of quiet time D_{LL}s is similar to that of the geomagnetic storm; D_{LL}^T generally has a steeper gradient as compared to existing models such that D_{LL}^T is larger at high L^* and smaller at low L^*. The steeper gradient in the D_{LL}s derived here is likely due to the use of a L^* and the TS05 model. The previous studies all used dipole L which does not vary with varying solar wind and geomagnetic conditions. Whereas with L^*, as activity increases the Earth's magnetic field is distorted resulting in changes in L^*. For example, during periods of enhanced solar wind and geomagnetic activity regions of high ULF wave power can be associated with lower L^* then would be in a dipole model; this leads to a steeper gradient in ULF wave power as a function of L^* then as a function of L. Overall, the steeper gradient here is likely to be more representative of the actual radial diffusion as it accounts for variations in the third adiabatic invariant L^*.

During the main phase of the storm D_{LL}^T is larger then D_{LL} Lejosne (2019) and smaller then the Ozeke et al. (2014), Brautigam and Albert (2000) D_{LL}s. And, prior to the storm onset, the D_{LL}s derived here are smaller at all L^* values then the existing models. These differences are likely a result of the parameterization used to quantify the D_{LL}s. Lejosne (2019) uses the magnetopause boundary defined by P_{dyn} and B_z to derive the magnetic field perturbations which drive radial diffusion. Both P_{dyn} and B_z are elevated for only a short period of time compared to $Sym\text{-}H$ and V_{sw} which is likely why the D_{LL}s derived here are larger then those of Lejosne (2019) during the main phase. With regard to the period prior to storm onset, Kp is elevated as compared to $Sym\text{-}H$, B_z, V_{sw}, and P_{dyn} which is likely why the Ozeke et al. (2014) and Brautigam and Albert (2000) D_{LL}s are larger then those derived here. These periods of elevated Kp are associate with enhanced AE driven by magnetospheric substorms. Though substorm activity leads to enhanced ULF waves in the form of short lived and irregular pulsations (Jacobs et al., 1964), the actual enhancement in Kp is the result of the larger substorm bays (Cramoysan et al., 1995) as opposed to ULF waves. Thus, its unclear whether this period would in fact lead to enhanced radial diffusion as depicted by the Ozeke et al. (2014) and Brautigam and Albert (2000) D_{LL}s as the resulting substorm-driven ULF wave activity is short lived. This difference is likely to propagate through any radial diffusion simulation leading to significant differences in the strength of radial transport and global topology of the radiation belt when using the different D_{LL}models.

Finally, it is important to note that D_{LL}^B, D_{LL}^E and total D_{LL} can reach rates greater then 10/day. Though this is in agreement with other models, as illustrated in **Error! Reference source not found.** (see also lifer et al., 2019; Sandhu et al., 2021), at these values the concept of radial diffusion will start to break down as electrons would be moving inward on time-scales on the order of or shorter than a drift period. In this regime coherent ULF wave-particle interactions may instead play an important role in the global dynamics of the outer radiation belt (e.g., Murphy 2020; 2018). The effect that enhanced ULF wave

power, which leads to these large D_{LL}s, and the effect they have on outer radiation belt is an important avenue of future research and which can be investigated with global models (Degeling et al., 2008, 2013, 2014; Komar et al., 2017).

In summary, we have used over 40 years of satellite data to calculate D_{LL}^{B} and D_{LL}^{E} over a range of L^* from 3-7 in non-dipole field using TS05. The diffusion rates are parameterised by an optimized set of solar wind and geomagnetic variables and provide diffusion coefficients at much higher time resolution and over a larger dynamic range then previous studies. The main results are:

- The gradient in our D_{LL}^{T} is generally steeper as compared to existing models, giving higher diffusion rates at larger L^* and lower rates at low L^*.
- D_{LL}^{E} is generally higher than D_{LL}^{B} at all L^* except during the main phase of storms.
- During the March 2013 magnetic storm D_{LL} generally agrees with previous work except for the initial phase of the storm where diffusion rates are lower at all L* < 5. We suggest that this is due to substorm activity which is captured in the Kp models and not in our new models.

The results are available for use in global radiation belt models to develop better reconstructions of the radiation belt environment (see Supporting Information for model coefficients). Future work will test both the model and model bias-removed D_{LL} performance in radiation belt simulations under varying geomagnetic conditions to determine if the new models improve the performance of radiation belt simulations as compared to existing D_{LL} models. In addition, future studies will investigate the performance of our new models as compared to existing models when using forecasted inputs. Finally, future studies will investigate including additional model inputs and independent variables and the time history of independent variables, along with more complex algorithms for regression as a path to improved D_{LL} models and radiation belt simulations.

Acknowledgments

This work is partly funded by UKRI grants ST/V006320/1 (STFC) and NE/P017185/2 and NE/V002554/2 (NERC); for the purpose of open access, the author has applied a Creative Commons Attribution (CC BY) license [where permitted by UKRI, 'Open Government Licence' or 'Creative Commons Attribution No-derivatives (CC BY-ND) license may be stated instead] to any Author Accepted Manuscript version arising. TD is supported by the Air Force Office of Scientific Research under award number FA9550-19-1-7039. SG and RBH were supported by NERC grant NE/V00249X/1 (Sat-Risk), NERC National Capability grants NE/R016038/1 and by NERC National Public Good activity grant NE/R016445/1. AJH and AB's contribution was funded by the Space Precipitation Impacts group, a NASA Goddard Internal Science Funding Model grant. IRM is supported by a Discovery Grant from Canadian NSERC, and by a UK Royal Society Wolfson Visiting Fellowship. LO is supported by the Canadian Space Agency.

Open Research

The THEMIS data is available via SPEDAS, PySPEDAS or the THEMIS data server, http://themis.ssl.berkeley.edu/data/themis. The GOES data is available from the NOAA National Centers for Environmental Information website, https://www.ngdc.noaa.gov/stp/satellite/goes/. Van Allen Probes data is available at the Coordinated Data Analysis Web (CDAWeb) https://cdaweb.gsfc.nasa.gov/.

The OMNI data is available at https://omniweb.gsfc.nasa.gov/. The higher level database used to develop the D_{LL} models is available via Zenodo, https://zenodo.org/record/7569732, doi: 10.5281/zenodo.7569732. The database contains two data sets, a magnetic field data set and an electric field data set. The magnetic field dataset contains the derived power spectral density for the compressional magnetic field $\boldsymbol{B}_{\parallel}$ from THEMIS, Van Allen Probes, and accompanying position (MLT, L, L* TS05), solar wind, and geomagnetic data. The electric field contains the derived power spectral density for the azimuthal electric field $\boldsymbol{E}_{\varphi}$ from THEMIS, Van Allen Probes, and GOES and accompanying position (MLT, L, L* TS05), solar wind, and geomagnetic data. See the Zenodo record for more description of the derived database and datasets.

Figures

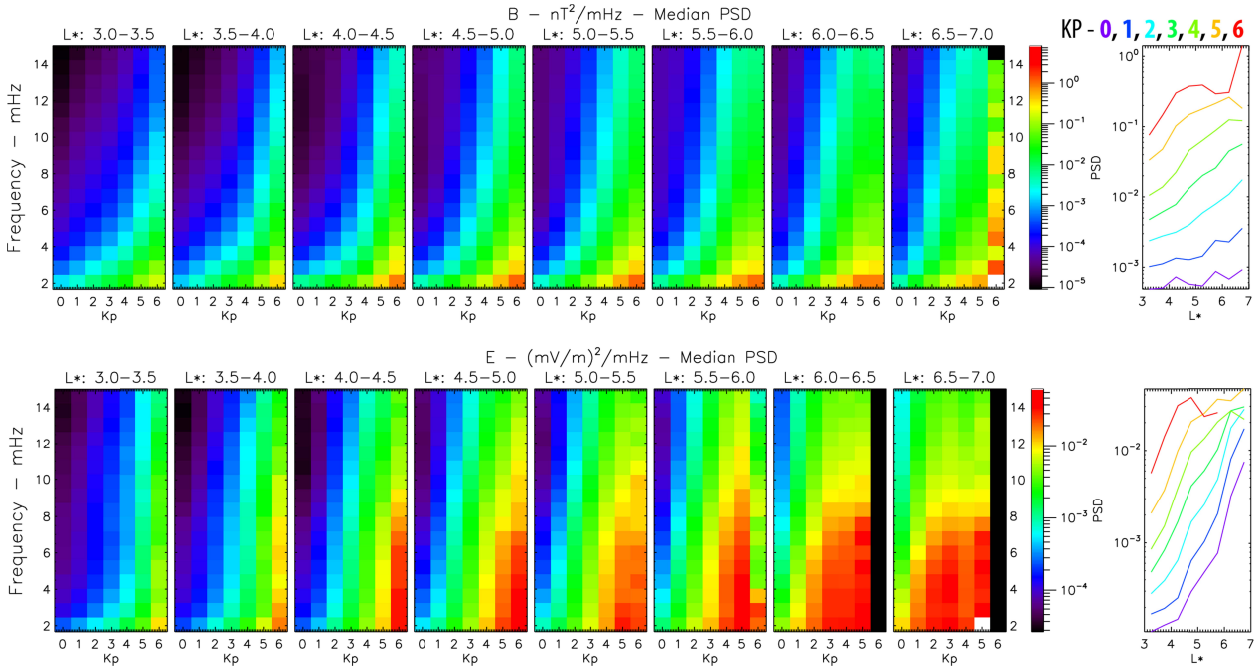

Figure 11: Statistical variation of the $\boldsymbol{B}_{\parallel}$ (top) and $\boldsymbol{E}_{\varphi}$(bottom) PSD. The spectral plots show the median PSD as a function of frequency (y-axis), Kp (x-axis) and L* (panels 1-8). The line plots show the variation of PSD at fixed a frequency of 2.5 mHz as a function of L* and Kp (color) for the entire dataset.

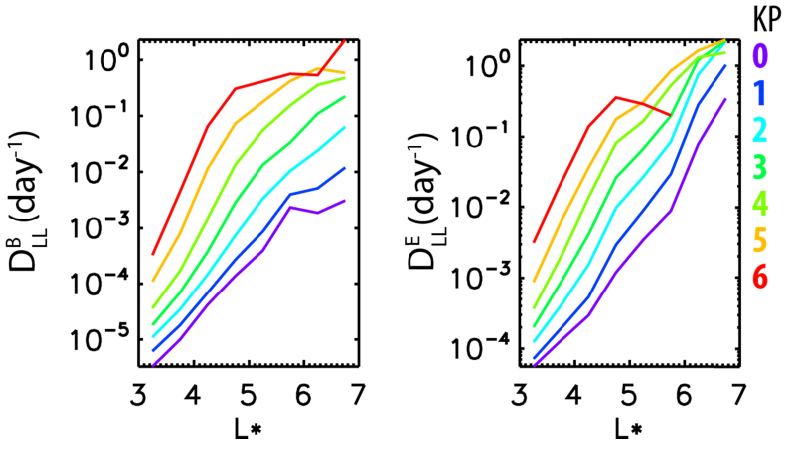

Figure 12: Median D_{LL}^{B} (left) and D_{LL}^{E}(right) as function of L* and Kp for the entire dataset.

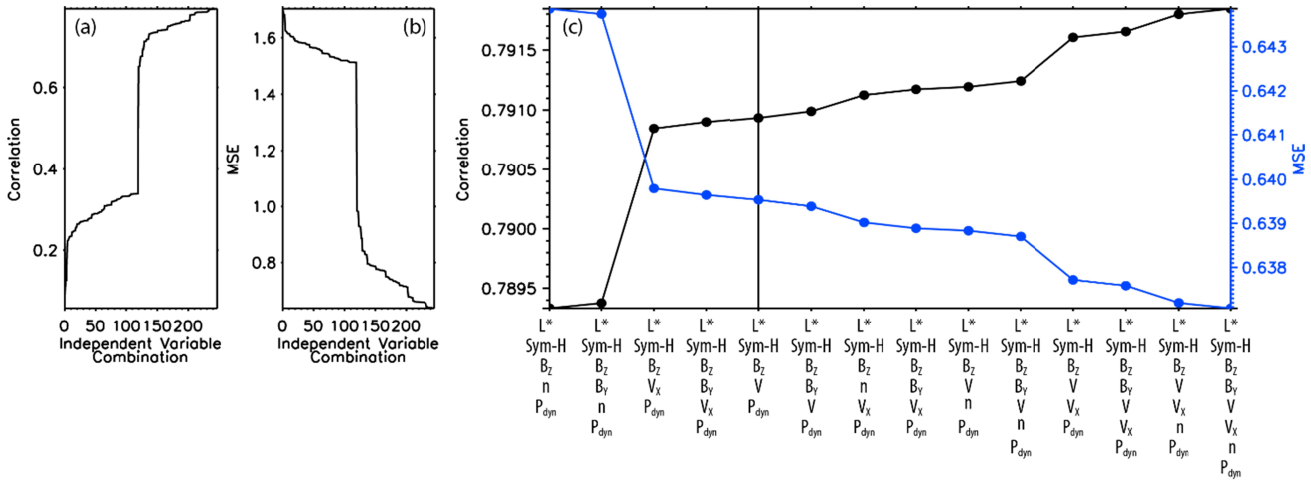

Figure 13: Results of the parametric study. (a) and (b) Correlation and mean square error (MSE) of data and multi-linear regression model for all combinations of independent variables (identified as integers on the x-axis). (c) A zoom in of (a) and (b) highlighting the combination of independent variables resulting in a high correlation and low MSE between the data and multi-linear regression model; the black line is the correlation and blue the MSE, the x-axis shows the various combinations of independent variables.

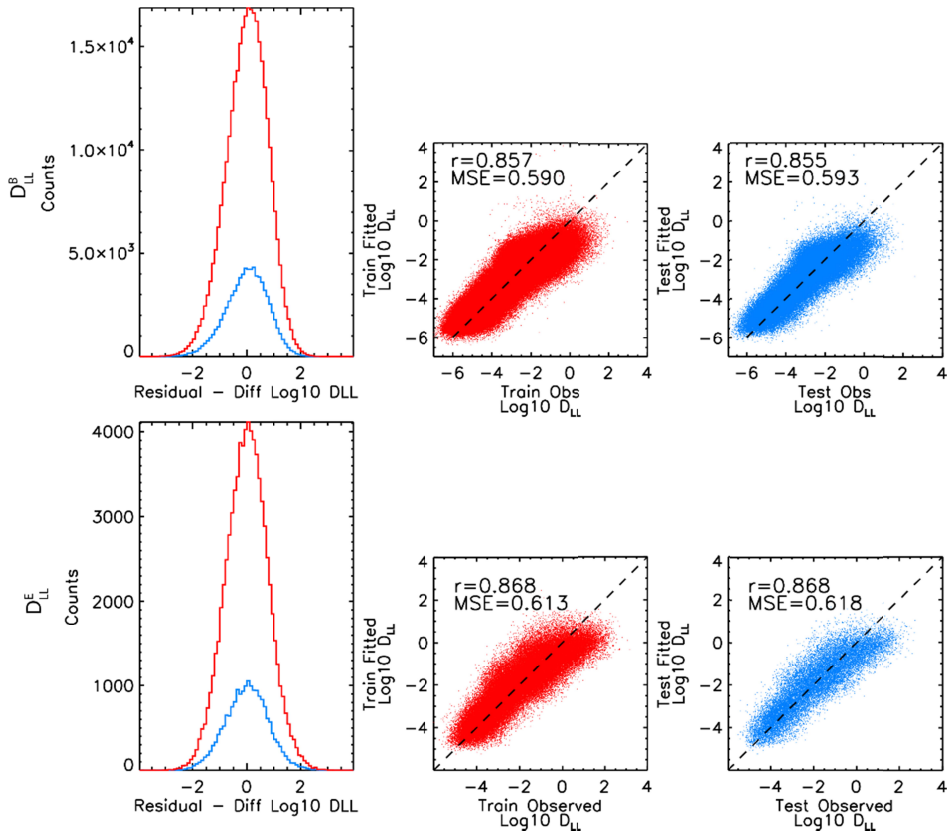

Figure 14: The residuals for the multi-linear regression D_{LL}^{B} and D_{LL}^{E} models (top and bottom). Right, distribution of the residuals for the train and test data sets (red and blue). Middle and right, observed D_{LL} versus modelled D_{LL} for the train and test data sets (blue and red); in each panel the correlation, r, and MSE are shown in the top left.

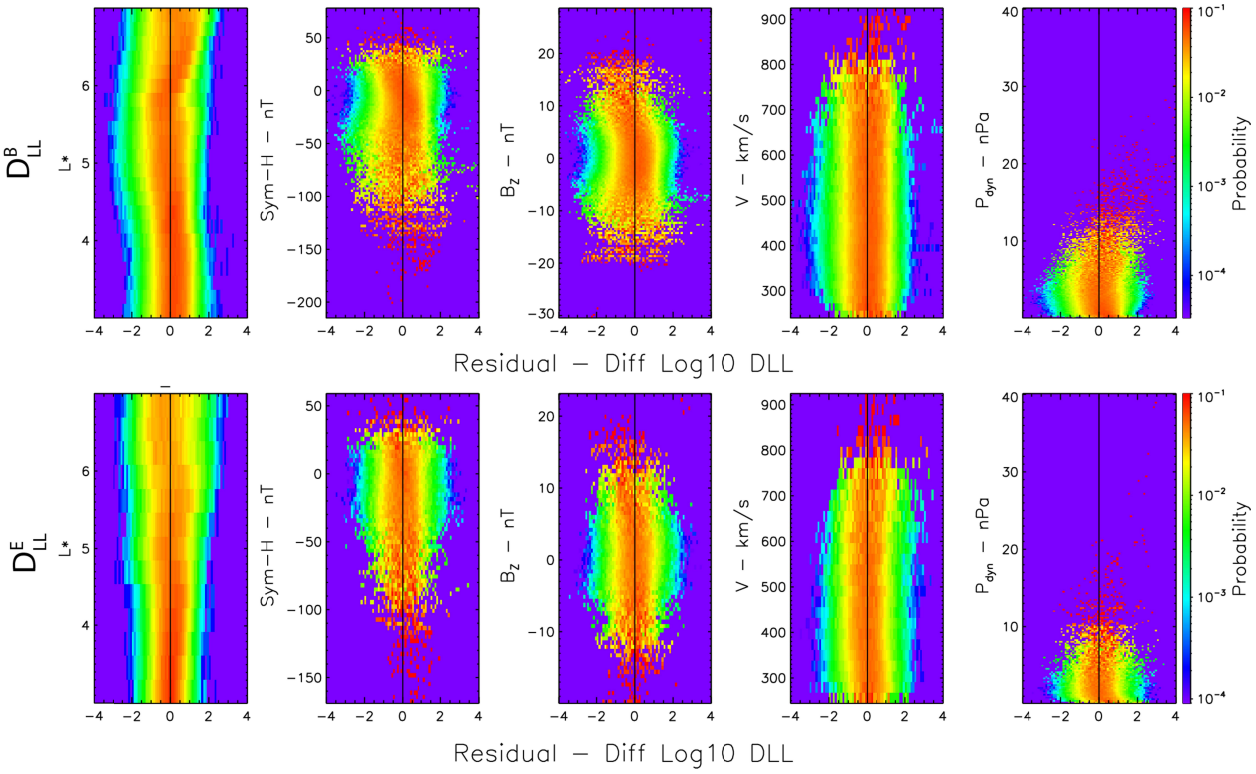

643

644 Figure 15: PDFs of the D^B_{LL} and D^E_{LL} model residuals calculated from the combined train and test data sets for each
645 of the independent variables.

646

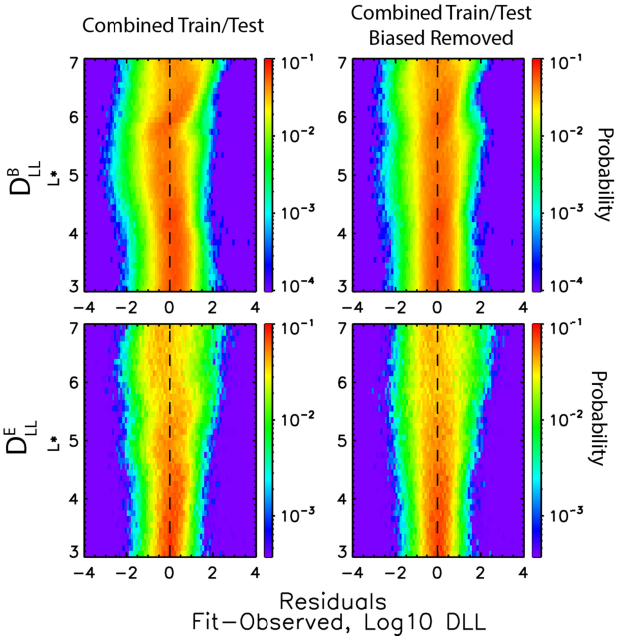

647

648 Figure 16: Comparison of the PDFs of both D^B_{LL} (top) and D^E_{LL} (bottom) model residuals (left) and residuals-biased-
649 removed (right) of the combined train/test datasets

650

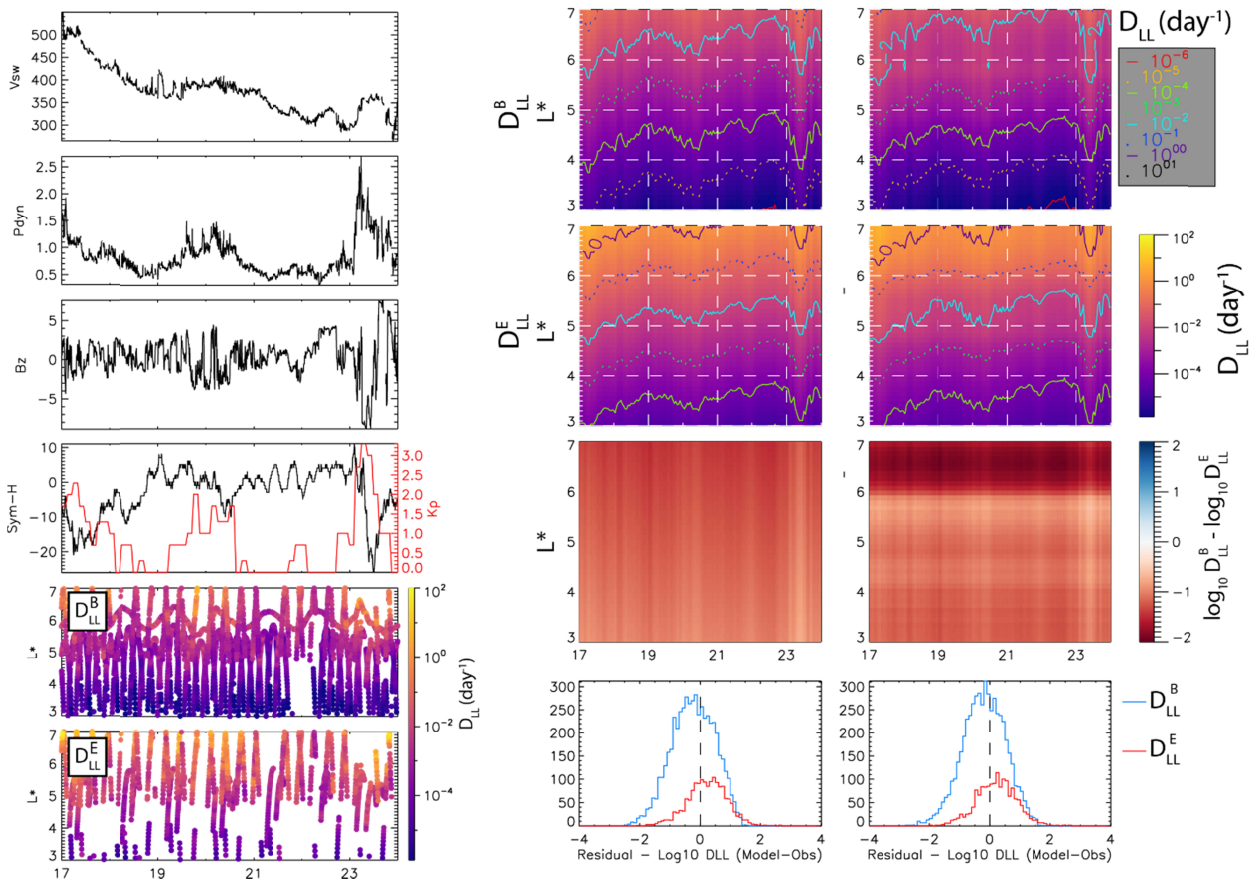

Figure 17: The modelled D_{LL}s during an interval of quiet solar wind and low geomagnetic activity. From top to bottom the left panel shows V, P_{dyn}, B_z, $Sym\text{-}H$ (black) and Kp (red), and the satellite derived D^B_{LL} and D^E_{LL}. The middle and right panel show the modelled and model-bias-removed D_{LL}s. From top to bottom the two right panels show D^B_{LL}, D^E_{LL}, the difference between the log of D^B_{LL} and D^E_{LL}, and then the model residuals calculated by comparing the modelled D_{LL}s to the satellite derived D_{LL}s. The contours in the top two panels are contours of constant D_{LL}, the white dashed lines are placed at major tick marks to aid in comparison between the model and model-bias-removed D_{LL}s.

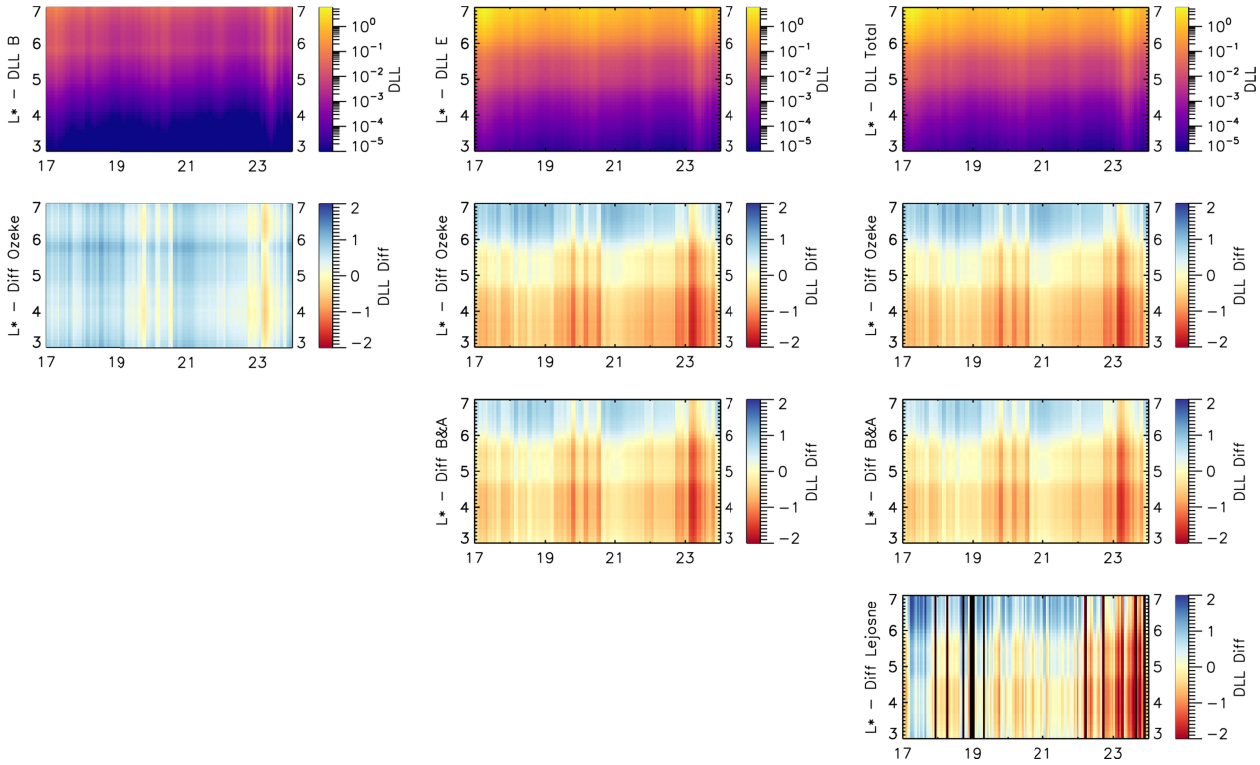

Figure 18: A comparison of bias-removed D_{LL}s derived here and those from Ozeke et al. (2014), Brautigam and Albert (2000), and Lejosne (2019). From left to right the columns show D_{LL}^{B}, D_{LL}^{E}, and $D_{LL}^{T} = D_{LL}^{B} + D_{LL}^{E}$. From top to bottom the rows show the modelled D_{LL}s derived here followed by the difference between the logs of modelled D_{LL}s and those from Ozeke et al. (2014), Brautigam and Albert (2000), and Lejosne (2019).

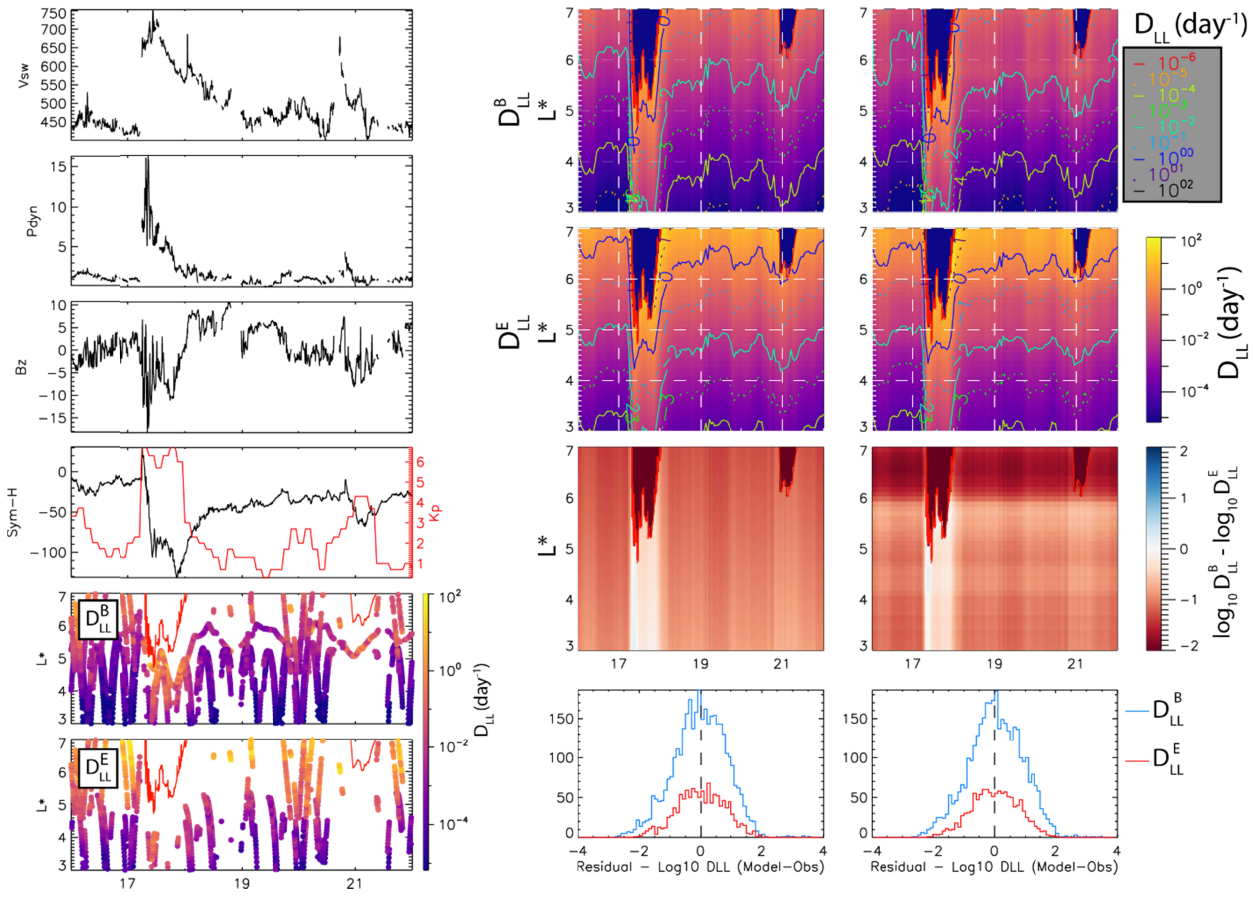

Figure 19: Solar wind dynamics, geomagnetic activity, satellite derived D_{LL}s, and modelled D_{LL}s during a geomagnetic storm in March 2013. The figure is in the same format as Figure 7. The red traces in the bottom two panels of the left column and top two panels of the middle and right column show the position of the last close drift shell throughout the interval.

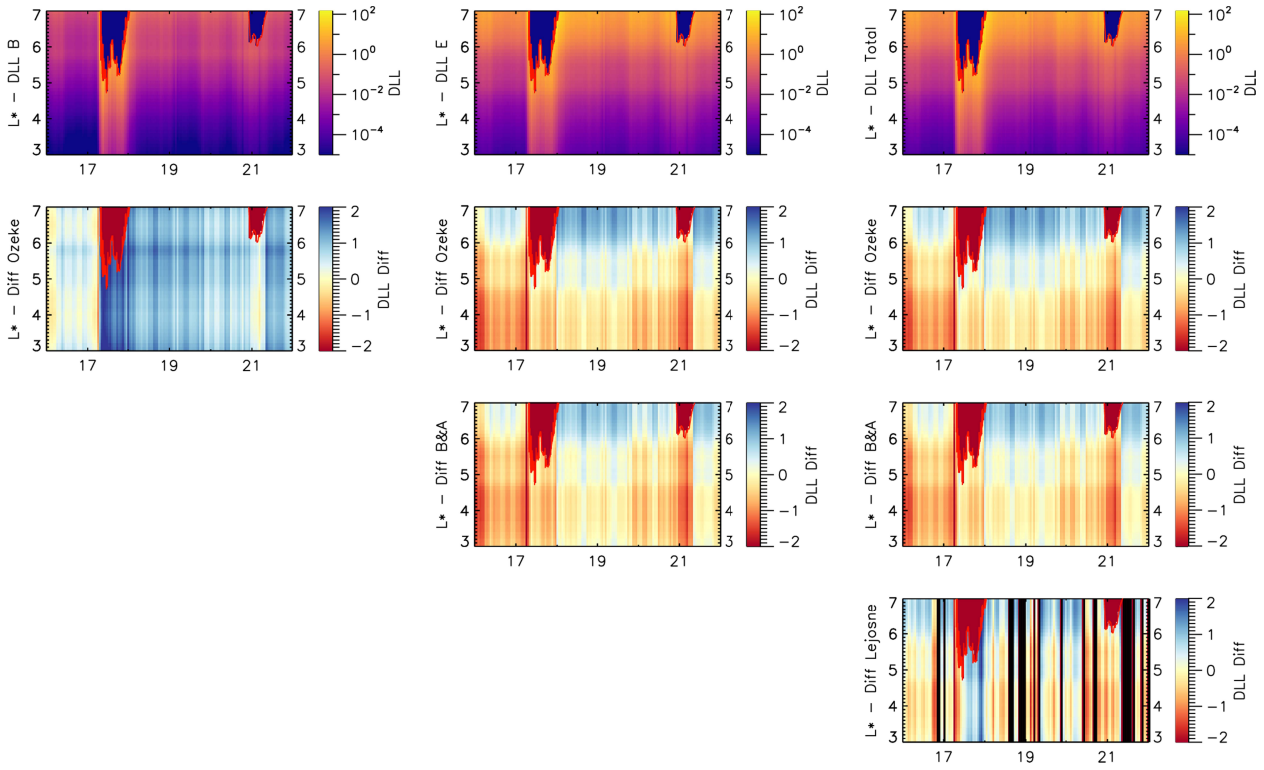

671

672 Figure 20: A comparison of the bias-removed D_{LL}s derived here and those from Ozeke et al. (2014), Brautigam and
673 Albert (2000), and Lejosne (2019) during a geomagnetic storm in March 2013. The figure is in the same format as
674 Figure 8. The red lines show the position of the last close drift shell throughout the interval.

675

References

Ali, A. F., Elkington, S. R., Tu, W., Ozeke, L. G., Chan, A. A., & Friedel, R. H. W. (2015). Magnetic field power spectra and magnetic radial diffusion coefficients using CRRES magnetometer data. *Journal of Geophysical Research: Space Physics*, *120*(2), 973–995. https://doi.org/10.1002/2014JA020419

Ali, A. F., Malaspina, D. M., Elkington, S. R., Jaynes, A. N., Chan, A. A., Wygant, J., & Kletzing, C. A. (2016). Electric and magnetic radial diffusion coefficients using the Van Allen probes data. *Journal of Geophysical Research: Space Physics*, *121*(10), 9586–9607. https://doi.org/10.1002/2016JA023002

Van Allen, J. A., & Frank, L. A. (1959). Radiation Around the Earth to a Radial Distance of 107,400 km. *Nature*, *183*(4659), 430–434. https://doi.org/10.1038/183430a0

Angelopoulos, V. (2008). The THEMIS mission. *Space Science Reviews*, *141*(1–4), 5–34. https://doi.org/10.1007/s11214-008-9336-1

Angelopoulos, V., Cruce, P., Drozdov, A., Grimes, E. W., Hatzigeorgiu, N., King, D. A., et al. (2019). The Space Physics Environment Data Analysis System (SPEDAS). *Space Science Reviews*, *215*(1), 9. https://doi.org/10.1007/s11214-018-0576-4

Baker, D N, Kanekal, S. G., Hoxie, V. C., Henderson, M. G., Li, X., Spence, H. E., et al. (2013). A long-lived relativistic electron storage ring embedded in Earth's outer Van Allen belt. *Science (New York, N.Y.)*, *340*(6129), 186–90. https://doi.org/10.1126/science.1233518

Baker, Daniel N. (2001). Satellite Anomalies due to Space Storms. In *Space Storms and Space Weather Hazards* (pp. 285–311). Dordrecht: Springer Netherlands. https://doi.org/10.1007/978-94-010-0983-6_11

Bentley, S. N., Watt, C. E. J., Owens, M. J., & Rae, I. J. (2018). ULF Wave Activity in the Magnetosphere: Resolving Solar Wind Interdependencies to Identify Driving Mechanisms. *Journal of Geophysical Research: Space Physics*, *123*(4), 2745–2771. https://doi.org/10.1002/2017JA024740

Bingley, L., Angelopoulos, V., Sibeck, D., Zhang, X., & Halford, A. (2019). The Evolution of a Pitch-Angle "Bite-Out" Scattering Signature Caused by EMIC Wave Activity: A Case Study. *Journal of Geophysical Research: Space Physics*, *124*(7), 5042–5055. https://doi.org/10.1029/2018JA026292

Borovsky, J. E., & Valdivia, J. A. (2018). The Earth's Magnetosphere: A Systems Science Overview and Assessment. *Surveys in Geophysics*, *39*(5), 817–859. https://doi.org/10.1007/s10712-018-9487-x

Bortnik, J., Chu, X., Ma, Q., Li, W., Zhang, X., Thorne, R. M., et al. (2018). Artificial Neural Networks for Determining Magnetospheric Conditions. In *Machine Learning Techniques for Space Weather* (pp. 279–300). Elsevier. https://doi.org/10.1016/B978-0-12-811788-0.00011-1

Boscher, D., Bourdarie, S., O'Brien, P., Guild, T., Heynderickx, D., Morley, S., et al. (2022). PRBEM/IRBEM: v5.0.0. https://doi.org/10.5281/ZENODO.6867768

Brautigam, D. H., & Albert, J. M. (2000). Radial diffusion analysis of outer radiation belt electrons during the October 9, 1990, magnetic storm. *Journal of Geophysical Research: Space Physics*, *105*(A1), 291–309. https://doi.org/10.1029/1999JA900344

713 Breneman, A. W., Halford, A., Millan, R., McCarthy, M., Fennell, J., Sample, J., et al. (2015). Global-scale
714 coherence modulation of radiation-belt electron loss from plasmaspheric hiss. *Nature*, *523*(7559),
715 193–195. https://doi.org/10.1038/nature14515

716 Breneman, A. W., Wygant, J. R., Tian, S., Cattell, C. A., Thaller, S. A., Goetz, K., et al. (2022). The Van Allen
717 Probes Electric Field and Waves Instrument: Science Results, Measurements, and Access to Data.
718 *Space Science Reviews*, *218*(8), 69. https://doi.org/10.1007/s11214-022-00934-y

719 Brito, T., Hudson, M. K., Kress, B., Paral, J., Halford, A., Millan, R., & Usanova, M. (2015). Simulation of
720 ULF wave-modulated radiation belt electron precipitation during the 17 March 2013 storm. *Journal*
721 *of Geophysical Research: Space Physics*, *120*(5), 3444–3461.
722 https://doi.org/10.1002/2014JA020838

723 Brizard, A. J., & Chan, A. A. (2001). Relativistic bounce-averaged quasilinear diffusion equation for low-
724 frequency electromagnetic fluctuations. *Physics of Plasmas*, *8*(11), 4762–4771.
725 https://doi.org/10.1063/1.1408623

726 Bruno, A., Blum, L. W., de Nolfo, G. A., Kataoka, R., Torii, S., Greeley, A. D., et al. (2022). EMIC-Wave
727 Driven Electron Precipitation Observed by CALET on the International Space Station. *Geophysical*
728 *Research Letters*, *49*(6). https://doi.org/10.1029/2021GL097529

729 Cassak, P. A., Emslie, A. G., Halford, A. J., Baker, D. N., Spence, H. E., Avery, S. K., & Fisk, L. A. (2017).
730 Space physics and policy for contemporary society. *Journal of Geophysical Research: Space Physics*,
731 *122*(4), 4430–4435. https://doi.org/10.1002/2017JA024219

732 Chaston, C. C., Bonnell, J. W., Halford, A. J., Reeves, G. D., Baker, D. N., Kletzing, C. A., & Wygant, J. R.
733 (2018). Pitch Angle Scattering and Loss of Radiation Belt Electrons in Broadband Electromagnetic
734 Waves. *Geophysical Research Letters*, *45*(18), 9344–9352. https://doi.org/10.1029/2018GL079527

735 Cramoysan, M., Bunting, R., & Orr, D. (1995). The use of a model current wedge in the determination of
736 the position of substorm current systems. *Annales Geophysicae*. https://doi.org/10.1007/s00585-
737 995-0583-0

738 Degeling, A. W., Ozeke, L. G., Rankin, R., Mann, I. R., & Kabin, K. (2008). Drift resonant generation of
739 peaked relativistic electron distributions by Pc 5 ULF waves. *Journal of Geophysical Research: Space*
740 *Physics*, *113*(2), 1–10. https://doi.org/10.1029/2007JA012411

741 Degeling, A. W., Rankin, R., Murphy, K., & Rae, I. J. (2013). Magnetospheric convection and
742 magnetopause shadowing effects in ULF wave-driven energetic electron transport. *Journal of*
743 *Geophysical Research: Space Physics*, *118*(6), 2919–2927. https://doi.org/10.1002/jgra.50219

744 Degeling, A. W., Rankin, R., & Zong, Q. G. (2014). Modeling radiation belt electron acceleration by ULF
745 fast mode waves, launched by solar wind dynamic pressure fluctuations. *Journal of Geophysical*
746 *Research: Space Physics*, *119*(11), 8916–8928. https://doi.org/10.1002/2013JA019672

747 Dimitrakoudis, S., Mann, I. R., Balasis, G., Papadimitriou, C., Anastasiadis, A., & Daglis, I. A. (2015).
748 Accurately specifying storm-time ULF wave radial diffusion in the radiation belts. *Geophysical*
749 *Research Letters*, *42*(14), 5711–5718. https://doi.org/10.1002/2015GL064707

750 Dimitrakoudis, S., Mann, I. R., Balasis, G., Papadimitriou, C., Anastasiadis, A., & Daglis, I. A. (2022). On
751 the Interplay Between Solar Wind Parameters and ULF Wave Power as a Function of Geomagnetic

752 Activity at High- and Mid-latitudes. *Journal of Geophysical Research: Space Physics*, *127*(1).
753 https://doi.org/10.1029/2021JA029693

754 Engebretson, M. J., Posch, J. L., Braun, D. J., Li, W., Ma, Q., Kellerman, A. C., et al. (2018). EMIC Wave
755 Events During the Four GEM QARBM Challenge Intervals. *Journal of Geophysical Research: Space*
756 *Physics*, *123*(8), 6394–6423. https://doi.org/10.1029/2018JA025505

757 Fei, Y., Chan, A. A., Elkington, S. R., & Wiltberger, M. J. (2006). Radial diffusion and MHD particle
758 simulations of relativistic electron transport by ULF waves in the September 1998 storm. *Journal of*
759 *Geophysical Research*, *111*(A12), A12209. https://doi.org/10.1029/2005JA011211

760 Glauert, S. A., Horne, R. B., & Kirsch, P. (2021). Evaluation of SaRIF High-Energy Electron Reconstructions
761 and Forecasts. *Space Weather*, *19*(12). https://doi.org/10.1029/2021SW002822

762 Halford, A. J., Garcia-Sage, K., Mann, I. R., Turner, D. L., & Breneman, A. W. (2022). The Effect of
763 Compression Induced Chorus Waves on 10s to 100s eV Electron Precipitation. *Geophysical*
764 *Research Letters*. https://doi.org/10.1029/2022GL098842

765 Horne, R. B. (2003). Resonant diffusion of radiation belt electrons by whistler-mode chorus. *Geophysical*
766 *Research Letters*, *30*(9), 1493. https://doi.org/10.1029/2003GL016963

767 Horne, Richard B., & Thorne, R. M. (1998). Potential waves for relativistic electron scattering and
768 stochastic acceleration during magnetic storms. *Geophysical Research Letters*, *25*(15), 3011–3014.
769 https://doi.org/10.1029/98GL01002

770 Horne, Richard B., Glauert, S. A., Kirsch, P., Heynderickx, D., Bingham, S., Thorn, P., et al. (2021). The
771 Satellite Risk Prediction and Radiation Forecast System (SaRIF). *Space Weather*, *19*(12).
772 https://doi.org/10.1029/2021SW002823

773 Horne, Richard B, Thorne, R. M., Shprits, Y. Y., Meredith, N. P., Glauert, S. A., Smith, A. J., et al. (2005).
774 Wave acceleration of electrons in the Van Allen radiation belts. *Nature*, *437*(7056), 227–30.
775 https://doi.org/10.1038/nature03939

776 Jacobs, J. A., Kato, Y., Matsushita, S., & Troitskaya, V. A. (1964). Classification of geomagnetic
777 micropulsations. *Journal of Geophysical Research*. https://doi.org/10.1029/JZ069i001p00180

778 Jonathan Rae, I., Murphy, K. R., Watt, C. E. J., Halford, A. J., Mann, I. R., Ozeke, L. G., et al. (2018). The
779 Role of Localized Compressional Ultra-low Frequency Waves in Energetic Electron Precipitation.
780 *Journal of Geophysical Research: Space Physics*, *123*(3), 1900–1914.
781 https://doi.org/10.1002/2017JA024674

782 Kanekal, S., & Miyoshi, Y. (2021). Dynamics of the terrestrial radiation belts: a review of recent results
783 during the VarSITI (Variability of the Sun and Its Terrestrial Impact) era, 2014–2018. *Progress in*
784 *Earth and Planetary Science*, *8*(1), 35. https://doi.org/10.1186/s40645-021-00413-y

785 Kepko, L., Spence, H. E., & Singer, H. J. (2002). ULF waves in the solar wind as direct drivers of
786 magnetospheric pulsations. *Geophysical Research Letters*, *29*(8), 39-1-39–4.
787 https://doi.org/10.1029/2001gl014405

788 King, J. H., & Papitashvili, N. E. (2005). Solar wind spatial scales in and comparisons of hourly Wind and
789 ACE plasma and magnetic field data. *Journal of Geophysical Research*, *110*(A2), A02104.

https://doi.org/10.1029/2004JA010649

Komar, C. M., Glocer, A., Hartinger, M. D., Murphy, K. R., Fok, M.-C., & Kang, S.-B. (2017). Electron Drift Resonance in the MHD-Coupled Comprehensive Inner Magnetosphere-Ionosphere Model. *Journal of Geophysical Research: Space Physics*, *122*(12). https://doi.org/10.1002/2017JA024163

Lejosne, S. (2019). Analytic Expressions for Radial Diffusion. *Journal of Geophysical Research: Space Physics*, *124*(6), 4278–4294. https://doi.org/10.1029/2019JA026786

Li, W., & Hudson, M. K. (2019). Earth's Van Allen Radiation Belts: From Discovery to the Van Allen Probes Era. *Journal of Geophysical Research: Space Physics*, *124*(11), 8319–8351. https://doi.org/10.1029/2018JA025940

Liu, W., Tu, W., Li, X., Sarris, T., Khotyaintsev, Y., Fu, H., et al. (2016). On the calculation of electric diffusion coefficient of radiation belt electrons with in situ electric field measurements by THEMIS. *Geophysical Research Letters*, *43*(3), 1023–1030. https://doi.org/10.1002/2015GL067398

Ma, Q., Li, W., Bortnik, J., Thorne, R. M., Chu, X., Ozeke, L. G., et al. (2018). Quantitative Evaluation of Radial Diffusion and Local Acceleration Processes During GEM Challenge Events. *Journal of Geophysical Research: Space Physics*, 1–15. https://doi.org/10.1002/2017JA025114

Mann, I. R., Ozeke, L. G., Murphy, K. R., Claudepierre, S. G., Turner, D. L., Baker, D. N., et al. (2016). Explaining the dynamics of the ultra-relativistic third Van Allen radiation belt. *Nature Physics*, (June), 1–6. https://doi.org/10.1038/nphys3799

Mathie, R. a, & Mann, I. R. (2001). On the solar wind control of Pc5 ULF pulsation power at mid-latitudes: Implications for MeV electron acceleration in the outer radiation belt. *Journal of Geophysical Research*, *106*. https://doi.org/10.1029/2001JA000002

Mauk, B. H., Fox, N. J., Kanekal, S. G., Kessel, R. L., Sibeck, D. G., & Ukhorskiy, a. (2013). Science objectives and rationale for the radiation belt storm probes mission. *Space Science Reviews*, *179*(1–4), 3–27. https://doi.org/10.1007/s11214-012-9908-y

Murphy, K. R., Mann, I. R., Rae, I. J., & Milling, D. K. (2011). Dependence of ground-based Pc5 ULF wave power on F10.7 solar radio flux and solar cycle phase. *Journal of Atmospheric and Solar-Terrestrial Physics*, *73*(11–12), 1500–1510. https://doi.org/10.1016/j.jastp.2011.02.018

Murphy, K. R., Rae, I. J., Mann, I. R., & Milling, D. K. (2011). On the nature of ULF wave power during nightside auroral activations and substorms: 1. Spatial distribution. *Journal of Geophysical Research: Space Physics*, *116*(A5), 1–12. https://doi.org/10.1029/2010JA015757

Murphy, K. R., Watt, C. E. J., Mann, I. R., Jonathan Rae, I., Sibeck, D. G., Boyd, A. J., et al. (2018). The Global Statistical Response of the Outer Radiation Belt During Geomagnetic Storms. *Geophysical Research Letters*, *45*(9), 3783–3792. https://doi.org/10.1002/2017GL076674

Murphy, K. R., Inglis, A. R., Sibeck, D. G., Watt, C. E. J., & Rae, I. J. (2020). Inner Magnetospheric ULF Waves: The Occurrence and Distribution of Broadband and Discrete Wave Activity. *Journal of Geophysical Research: Space Physics*, *125*(9), 1–18. https://doi.org/10.1029/2020JA027887

Murphy, K.R., Inglis, A. R., Sibeck, D. G., Rae, I. J., Watt, C. E. J., Silveira, M., et al. (2018). Determining the Mode, Frequency, and Azimuthal Wave Number of ULF Waves During a HSS and Moderate

Geomagnetic Storm. *Journal of Geophysical Research: Space Physics*, *123*(8). https://doi.org/10.1029/2017JA024877

Murphy, Kyle R., Mann, I. R., & Sibeck, D. G. (2015). On the dependence of storm-time ULF wave power on magnetopause location: Impacts for ULF wave radial diffusion. *Geophysical Research Letters*, n/a-n/a. https://doi.org/10.1002/2015GL066592

Murphy, Kyle R., Mann, I. R., Sibeck, D. G., Rae, I. J., Watt, C. E. J., Ozeke, L. G., et al. (2020). A Framework for Understanding and Quantifying the Loss and Acceleration of Relativistic Electrons in the Outer Radiation Belt During Geomagnetic Storms. *Space Weather*, *18*(5). https://doi.org/10.1029/2020SW002477

Niehof, J., Morley, S., jnlanl, spacecataz, Haiducek, J., AntoineBrunet, et al. (2022). spacepy/spacepy: 0.3.0. https://doi.org/10.5281/ZENODO.6499545

O'Brien, T. P., Looper, M. D., & Blake, J. B. (2004). Quantification of relativistic electron microburst losses during the GEM storms. *Geophysical Research Letters*, *31*(4), 2–5. https://doi.org/10.1029/2003GL018621

Olifer, L., Mann, I. R., Morley, S. K., Ozeke, L. G., & Choi, D. (2018). On the Role of Last Closed Drift Shell Dynamics in Driving Fast Losses and Van Allen Radiation Belt Extinction. *Journal of Geophysical Research: Space Physics*, *123*(5), 3692–3703. https://doi.org/10.1029/2018JA025190

Olifer, L., Mann, I. R., Ozeke, L. G., Rae, I. J., & Morley, S. K. (2019). On the Relative Strength of Electric and Magnetic ULF Wave Radial Diffusion During the March 2015 Geomagnetic Storm. *Journal of Geophysical Research: Space Physics*, *124*(4), 2569–2587. https://doi.org/10.1029/2018JA026348

Ozeke, L. G., Mann, I. R., Murphy, K. R., Rae, I. J., & Chan, A. A. (2013). ULF Wave-Driven Radial Diffusion Simulations of the Outer Radiation Belt. In *Geophysical Monograph Series* (Vol. 199, pp. 139–150). https://doi.org/10.1029/2012GM001332

Ozeke, L. G., Mann, I. R., Claudepierre, S. G., Henderson, M., Morley, S. K., Murphy, K. R., et al. (2019). The March 2015 Superstorm Revisited: Phase Space Density Profiles and Fast ULF Wave Diffusive Transport. *Journal of Geophysical Research: Space Physics*, *124*(2), 1143–1156. https://doi.org/10.1029/2018JA026326

Ozeke, L. G., Mann, I. R., Olifer, L., Dufresne, K. Y., Morley, S. K., Claudepierre, S. G., et al. (2020). Rapid Outer Radiation Belt Flux Dropouts and Fast Acceleration During the March 2015 and 2013 Storms: The Role of Ultra-Low Frequency Wave Transport From a Dynamic Outer Boundary. *Journal of Geophysical Research: Space Physics*, *125*(2), 1–20. https://doi.org/10.1029/2019ja027179

Ozeke, L. G. L. G., Mann, I. R. I. R., Murphy, K. R. K. R., Jonathan Rae, I., & Milling, D. K. D. K. (2014). Analytic expressions for ULF wave radiation belt radial diffusion coefficients. *Journal of Geophysical Research: Space Physics*, *119*(3), 1587–1605. https://doi.org/10.1002/2013JA019204

Ozeke, Louis G., Mann, I. R., Murphy, K. R., Jonathan Rae, I., & Milling, D. K. (2014). Analytic expressions for ULF wave radiation belt radial diffusion coefficients. *Journal of Geophysical Research: Space Physics*, *119*(3), 1587–1605. https://doi.org/10.1002/2013JA019204

Ozeke, Louis G., Mann, I. R., Turner, D. L., Murphy, K. R., Degeling, A. W., Rae, I. J., & Milling, D. K. (2014). Modeling cross L shell impacts of magnetopause shadowing and ULF wave radial diffusion in the

867 Van Allen belts. *Geophysical Research Letters*, *41*(19), 6556–6562.
868 https://doi.org/10.1002/2014GL060787

869 Ozeke, Louis G., Mann, I. R., Murphy, K. R., Sibeck, D. G., & Baker, D. N. (2017). Ultra-relativistic
870 Radiation Belt Extinction and ULF Wave Radial Diffusion: Modeling the September 2014 Extended
871 Dropout Event. *Geophysical Research Letters*, (September), 1–10.
872 https://doi.org/10.1002/2017GL072811

873 Rae, I. Jonathan, Mann, I. R., Murphy, K. R., Ozeke, L. G., Milling, D. K., Chan, A. a., et al. (2012). Ground-
874 based magnetometer determination of in situ Pc4-5 ULF electric field wave spectra as a function of
875 solar wind speed. *Journal of Geophysical Research: Space Physics*, *117*(4), 1–17.
876 https://doi.org/10.1029/2011JA017335

877 Rae, I.J., Murphy, K. R., Watt, C. E. J., Sandhu, J. K., Georgiou, M., Degeling, A. W., et al. (2019). How Do
878 Ultra-Low Frequency Waves Access the Inner Magnetosphere During Geomagnetic Storms?
879 *Geophysical Research Letters*, *46*(19). https://doi.org/10.1029/2019GL082395

880 Rae, J., Forsyth, C., Dunlop, M., Palmroth, M., Lester, M., Friedel, R., et al. (2022). What are the
881 fundamental modes of energy transfer and partitioning in the coupled Magnetosphere-Ionosphere
882 system? *Experimental Astronomy*. https://doi.org/10.1007/s10686-022-09861-w

883 Reeves, G. D., Spence, H. E., Henderson, M. G., Morley, S. K., Friedel, R. H. W., Funsten, H. O., et al.
884 (2013). Electron acceleration in the heart of the Van Allen radiation belts. *Science*, *341*(6149), 991–
885 994. https://doi.org/10.1126/science.1237743

886 Sandhu, J. K., Rae, I. J., Wygant, J. R., Breneman, A. W., Tian, S., Watt, C. E. J., et al. (2021). ULF Wave
887 Driven Radial Diffusion During Geomagnetic Storms: A Statistical Analysis of Van Allen Probes
888 Observations. *Journal of Geophysical Research: Space Physics*, *126*(4).
889 https://doi.org/10.1029/2020JA029024

890 Schulz, M., & Lanzerotti, L. J. (1974). Particle diffusion in the radiation belts. *Pdrb*.

891 Sibeck, D. G., & Angelopoulos, V. (2008). THEMIS Science Objectives and Mission Phases. *Space Science*
892 *Reviews*, *141*(1–4), 35–59. https://doi.org/10.1007/s11214-008-9393-5

893 Singer, H., Matheson, L., Grubb, R., Newman, A., & Bouwer, D. (1996). Monitoring space weather with
894 the GOES magnetometers. In E. R. Washwell (Ed.), *GOES-8 and Beyond* (Vol. 2812, pp. 299–308).
895 SPIE. https://doi.org/10.1117/12.254077

896 Staples, F. A., Kellerman, A., Murphy, K. R., Rae, I. J., Sandhu, J. K., & Forsyth, C. (2022). Resolving
897 Magnetopause Shadowing Using Multimission Measurements of Phase Space Density. *Journal of*
898 *Geophysical Research: Space Physics*, *127*(2). https://doi.org/10.1029/2021JA029298

899 Thorne, R. M., Li, W., Ni, B., Ma, Q., Bortnik, J., Chen, L., et al. (2013). Rapid local acceleration of
900 relativistic radiation-belt electrons by magnetospheric chorus. *Nature*, *504*(7480), 411–414.
901 https://doi.org/10.1038/nature12889

902 Tsyganenko, N. A., & Sitnov, M. I. (2005). Modeling the dynamics of the inner magnetosphere during
903 strong geomagnetic storms. *Journal of Geophysical Research*, *110*(A3), A03208.
904 https://doi.org/10.1029/2004JA010798

905 Turner, D. L., Shprits, Y., Hartinger, M., & Angelopoulos, V. (2012). Explaining sudden losses of outer
906 radiation belt electrons during geomagnetic storms. *Nature Physics*, *8*(3), 208–212.
907 https://doi.org/10.1038/nphys2185

908 WEST, H. I., BUCK, R. M., & WALTON, J. R. (1972). Shadowing of Electron Azimuthal-Drift Motions near
909 the Noon Magnetopause. *Nature Physical Science*, *240*(97), 6–7.
910 https://doi.org/10.1038/physci240006a0

911

Figure 1.

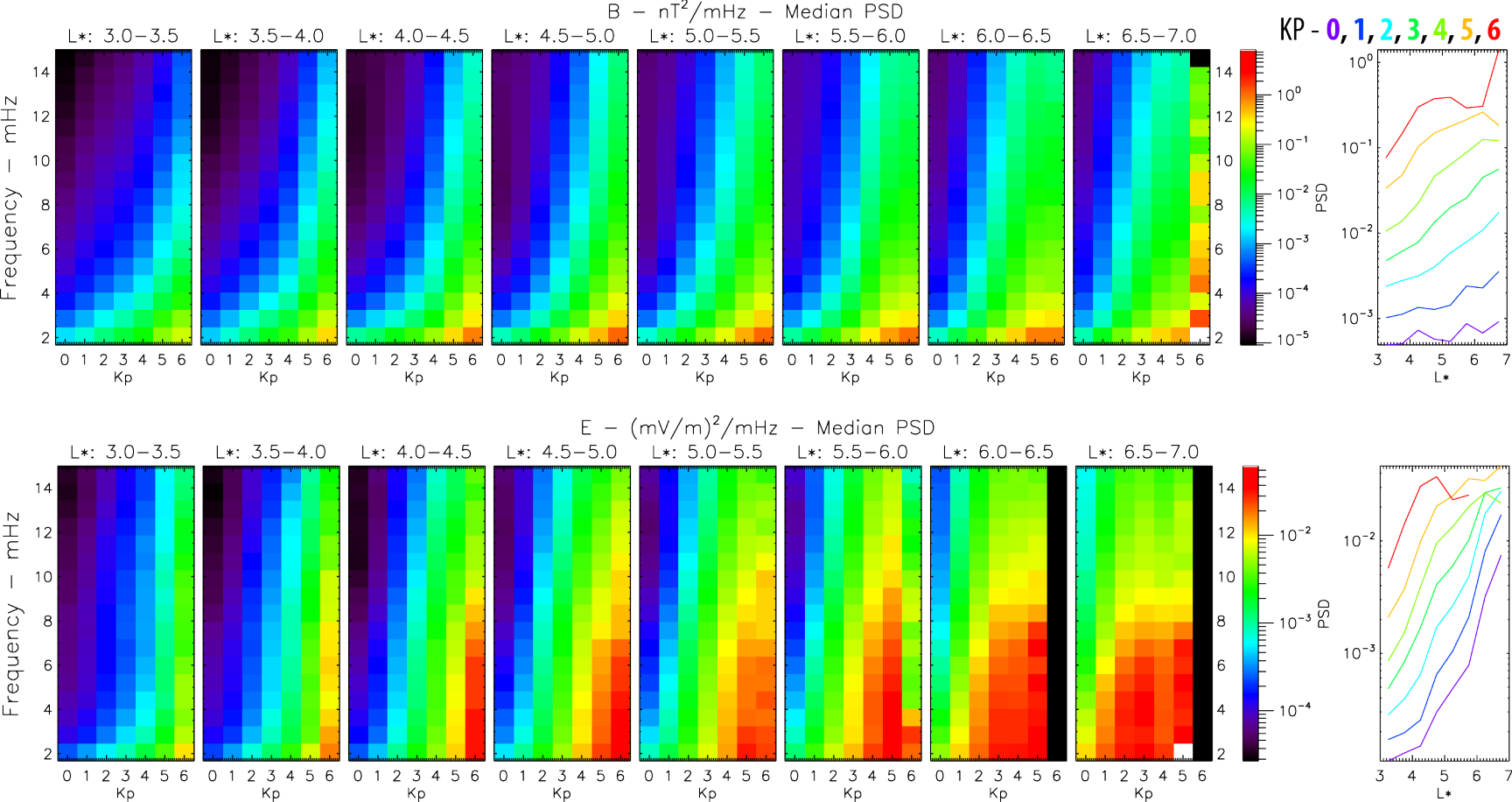
B – nT²/mHz – Median PSD
L*: 3.0–3.5
L*: 3.5–4.0
L*: 4.0–4.5
L*: 4.5–5.0
L*: 5.0–5.5
L*: 5.5–6.0
L*: 6.0–6.5
L*: 6.5–7.0
KP - 0, 1, 2, 3, 4, 5, 6
Frequency – mHz
Kp
PSD
L*
E – (mV/m)²/mHz – Median PSD

Figure 2.

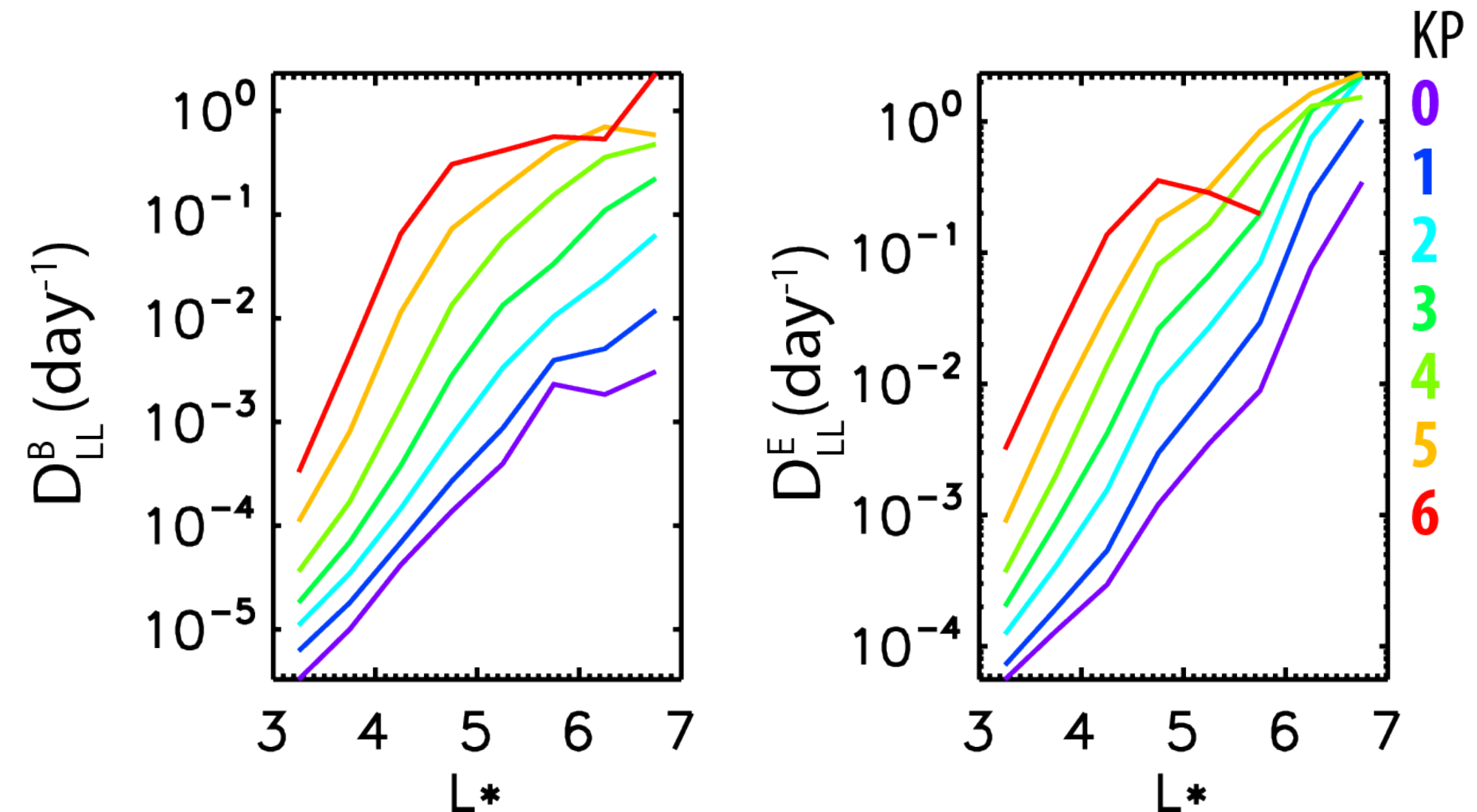
KP
0
1
2
3
4
5
6
D^B_{LL} (day^{-1})
10^0
10^{-1}
10^{-2}
10^{-3}
10^{-4}
10^{-5}
3
4
5
6
7
L*
D^E_{LL} (day^{-1})
10^0
10^{-1}
10^{-2}
10^{-3}
10^{-4}
3
4
5
6
7
L*

Figure 3.

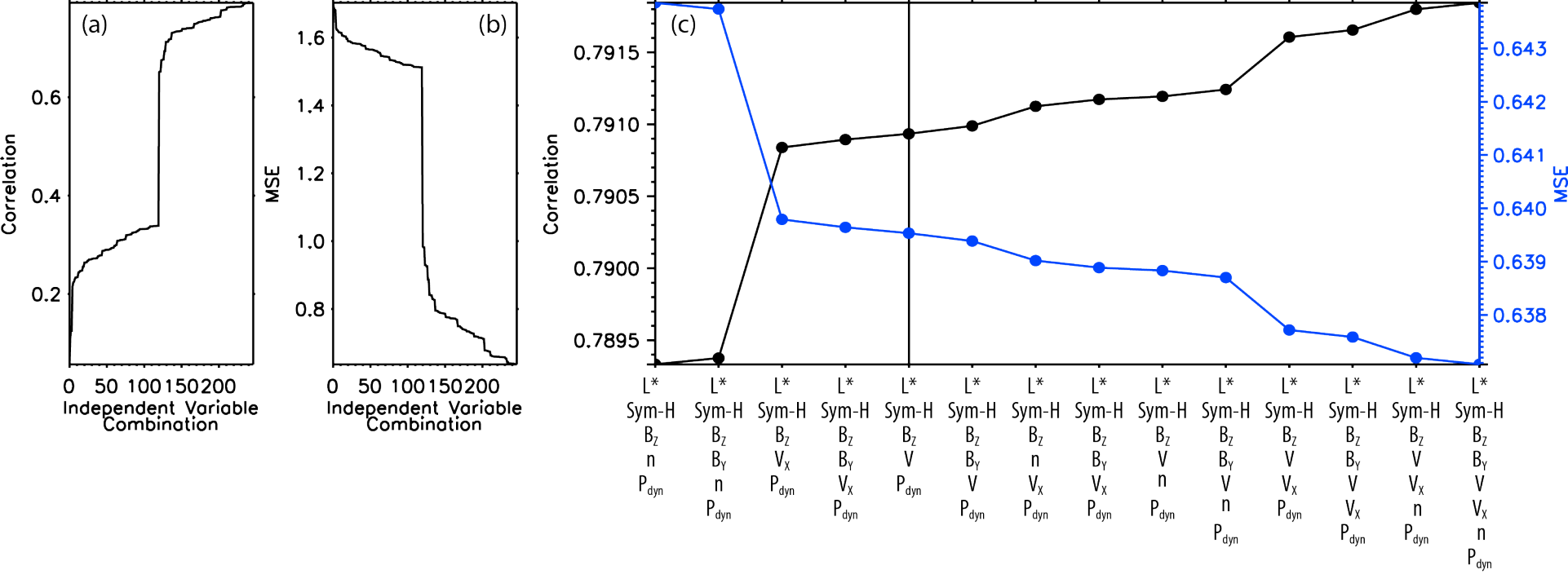
(a)
Correlation
0.2
0.4
0.6
0 50 100 150 200
Independent Variable Combination
(b)
MSE
0.8
1.0
1.2
1.4
1.6
0 50 100 150 200
Independent Variable Combination
(c)
Correlation
0.7895
0.7900
0.7905
0.7910
0.7915
MSE
0.638
0.639
0.640
0.641
0.642
0.643
L* Sym-H Bz n Pdyn
L* Sym-H Bz BY n Pdyn
L* Sym-H Bz VX Pdyn
L* Sym-H Bz BY VX Pdyn
L* Sym-H Bz V Pdyn
L* Sym-H Bz BY V Pdyn
L* Sym-H Bz n VX Pdyn
L* Sym-H Bz BY VX Pdyn
L* Sym-H Bz V n Pdyn
L* Sym-H Bz BY V n Pdyn
L* Sym-H Bz V VX Pdyn
L* Sym-H Bz BY V VX Pdyn
L* Sym-H Bz V VX n Pdyn
L* Sym-H Bz BY V VX n Pdyn

Figure 4.

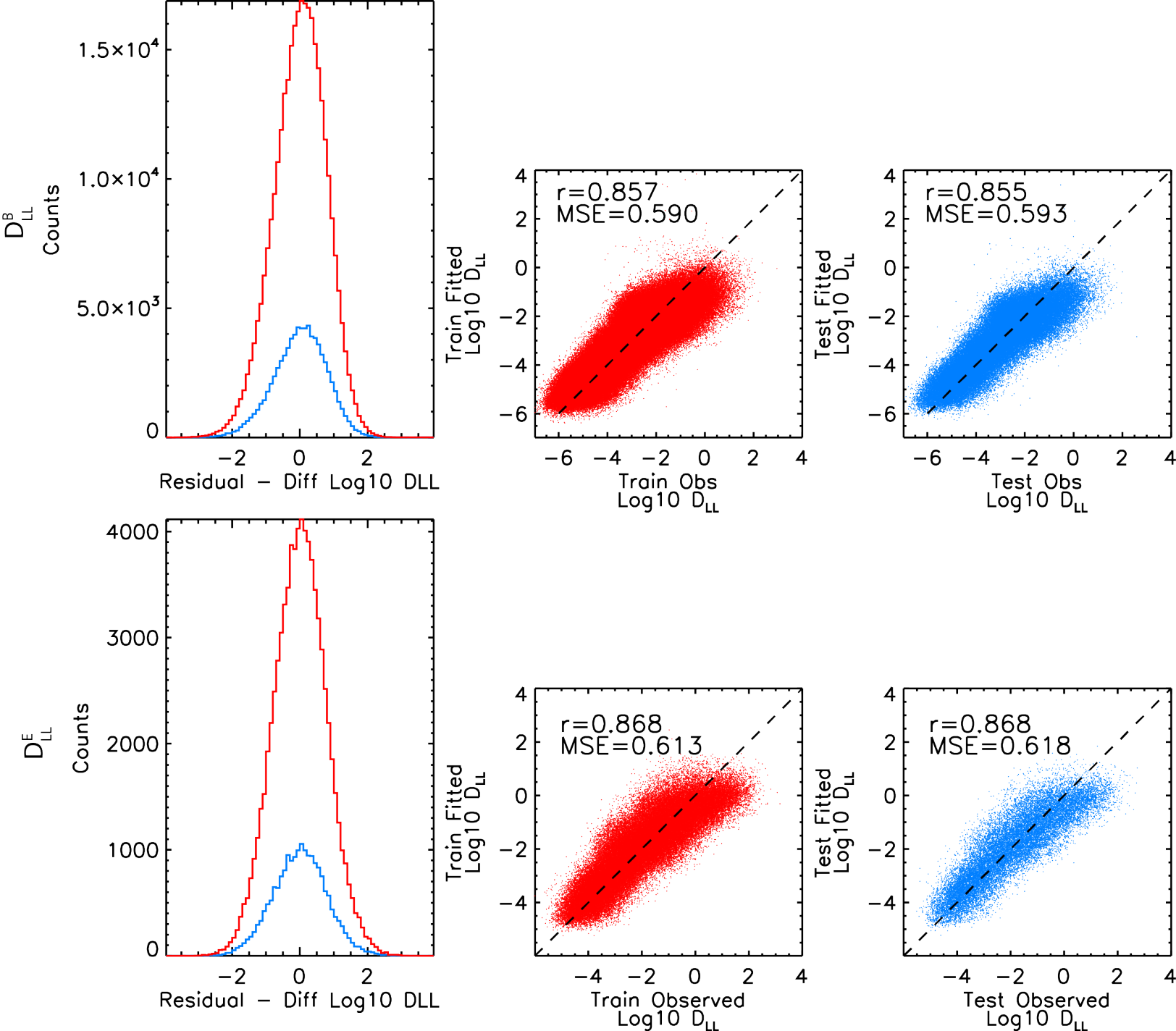
D^B_{LL}
Counts
1.5×10^4
1.0×10^4
5.0×10^3
0
−2
0
2
Residual − Diff Log10 DLL
Train Fitted Log10 D_{LL}
r=0.857
MSE=0.590
Train Obs Log10 D_{LL}
Test Fitted Log10 D_{LL}
r=0.855
MSE=0.593
Test Obs Log10 D_{LL}
D^E_{LL}
Counts
4000
3000
2000
1000
0
Residual − Diff Log10 DLL
Train Fitted Log10 D_{LL}
r=0.868
MSE=0.613
Train Observed Log10 D_{LL}
Test Fitted Log10 D_{LL}
r=0.868
MSE=0.618
Test Observed Log10 D_{LL}

Figure 5.

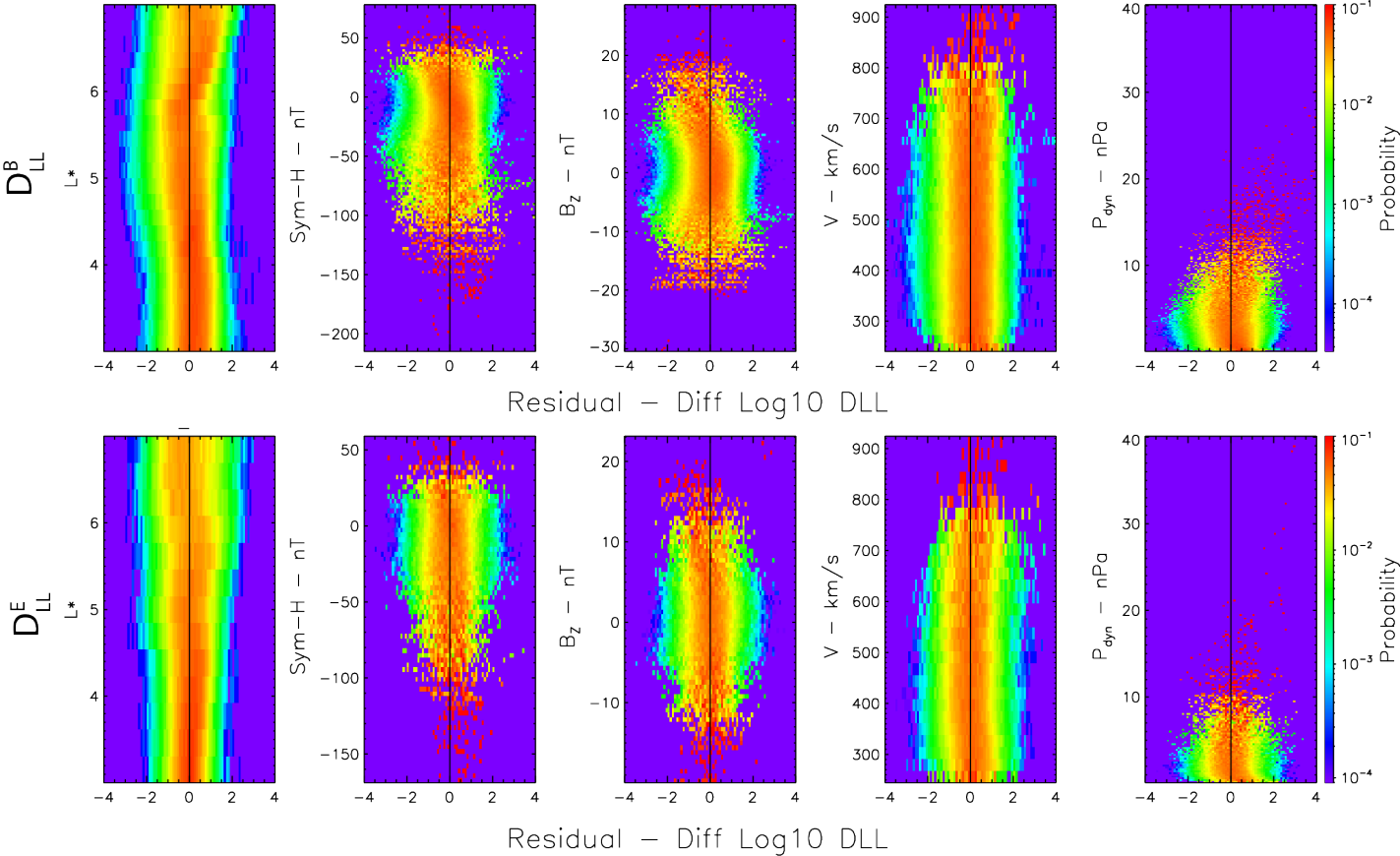
D^B_{LL}
D^E_{LL}
L*
Sym−H − nT
B_z − nT
V − km/s
P_{dyn} − nPa
Probability
Residual − Diff Log10 DLL
Residual − Diff Log10 DLL

Figure 6.

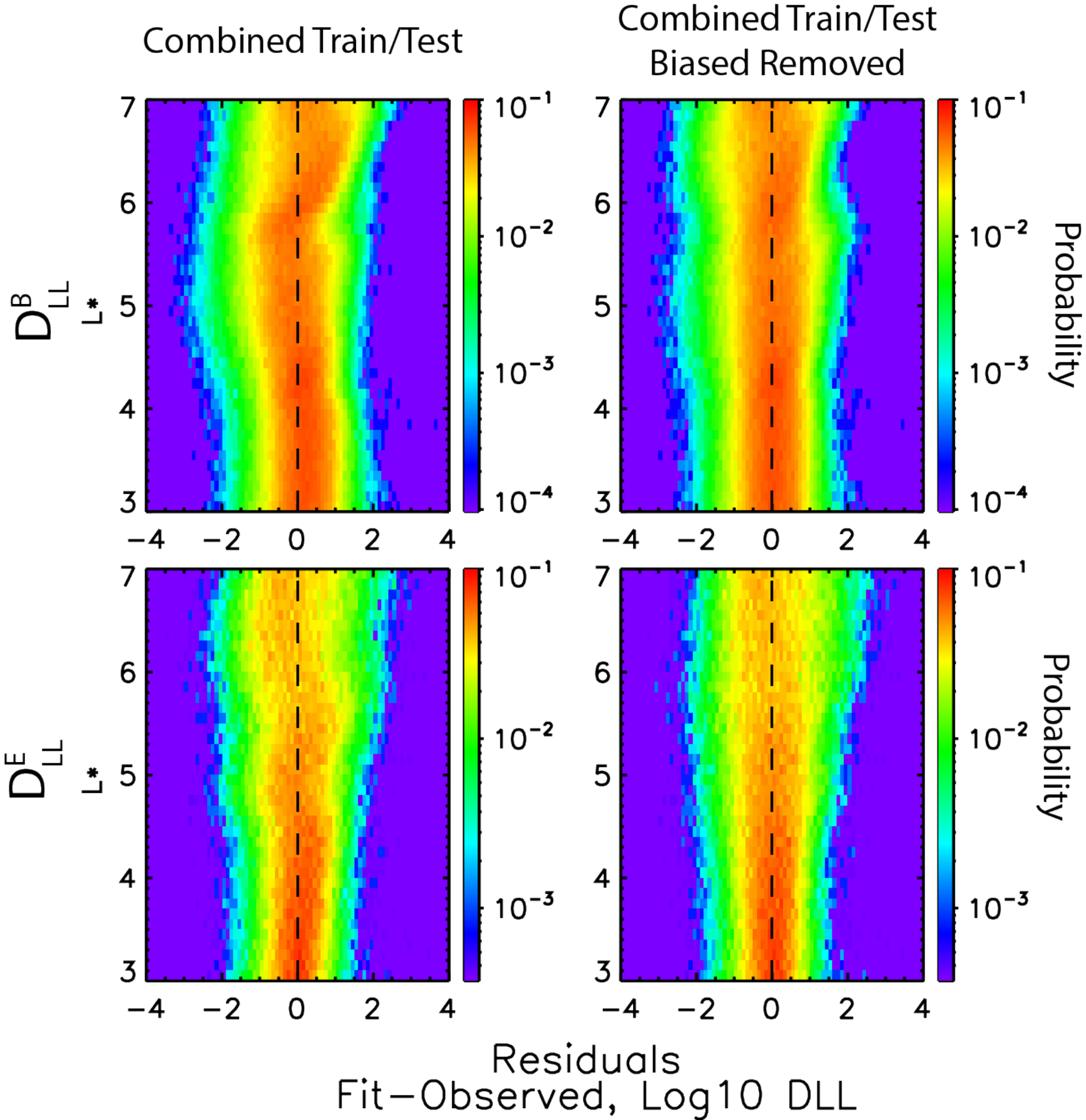
Combined Train/Test
Combined Train/Test
Biased Removed
D^B_{LL}
D^E_{LL}
L*
7
6
5
4
3
−4
−2
0
2
4
10^{-1}
10^{-2}
10^{-3}
10^{-4}
Probability
Residuals
Fit−Observed, Log10 DLL

Figure 7.

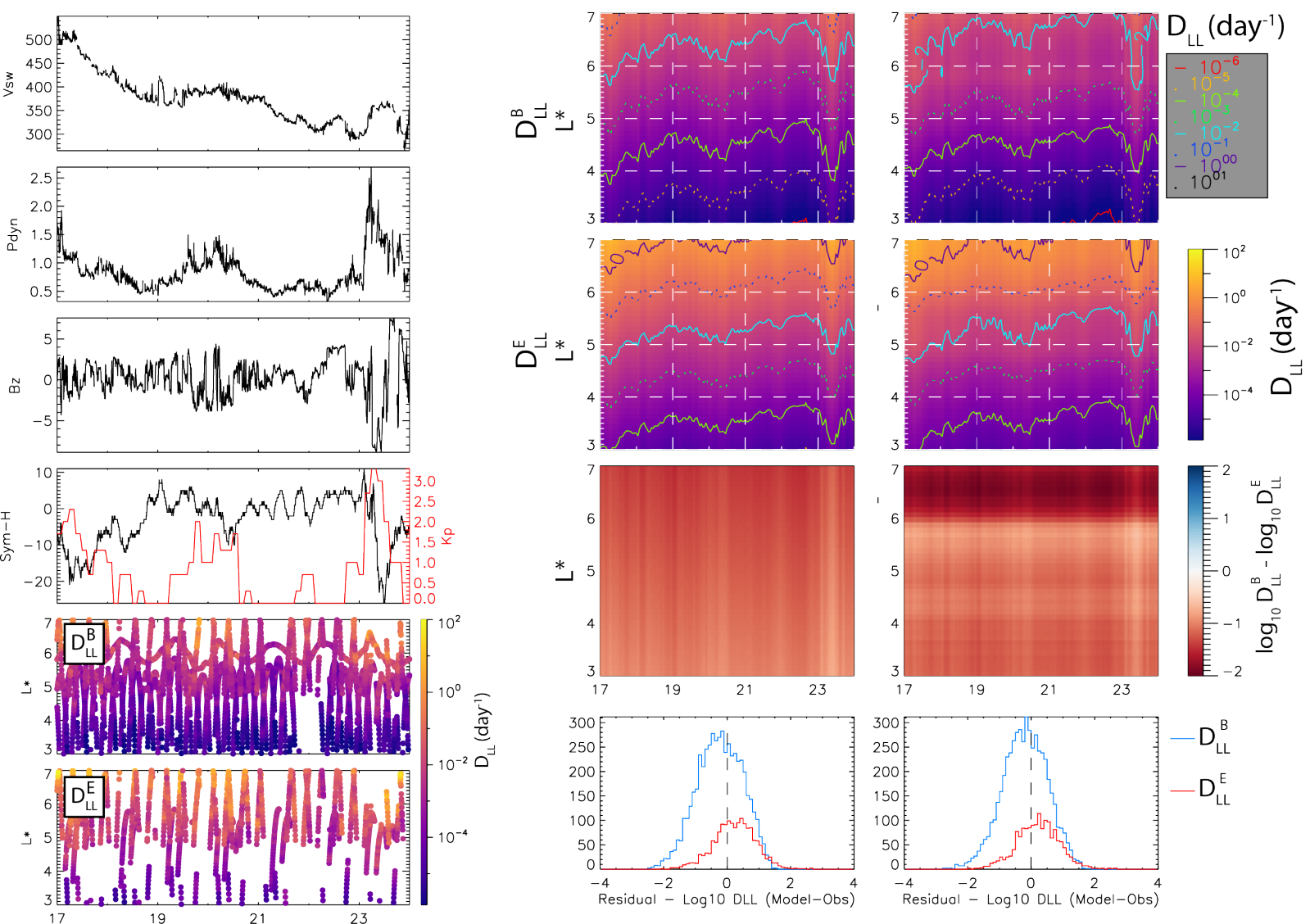
Vsw
Pdyn
Bz
Sym-H
Kp
D^B_{LL}
D^E_{LL}
L*
D_{LL} (day^{-1})
D_{LL} (day^{-1})
$\log_{10} D^B_{LL} - \log_{10} D^E_{LL}$
Residual = Log10 DLL (Model−Obs)
Residual = Log10 DLL (Model−Obs)
D^B_{LL}
D^E_{LL}

Figure 8.

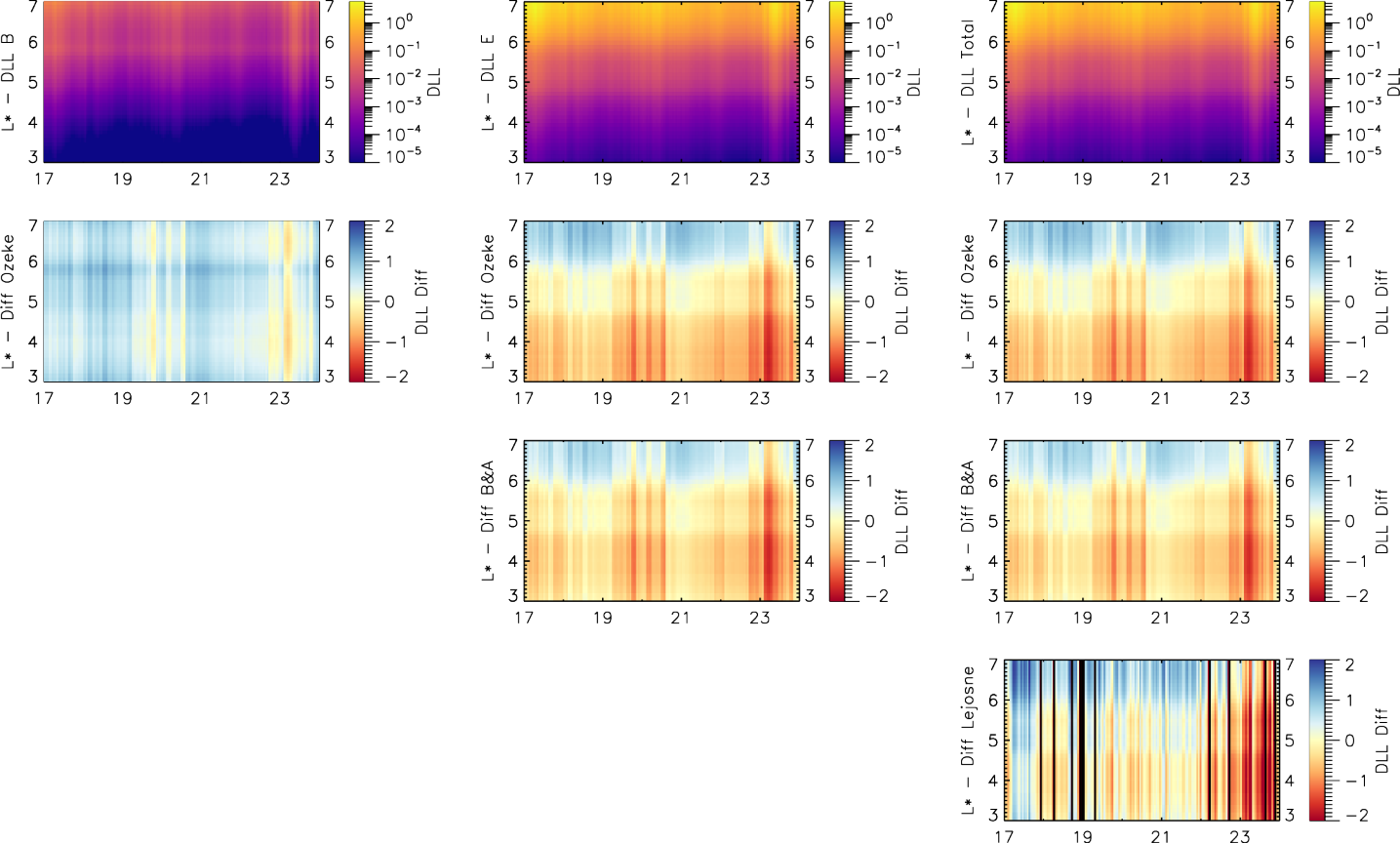
L* – DLL B
L* – DLL E
L* – DLL Total
L* – Diff Ozeke
L* – Diff B&A
L* – Diff Lejosne
DLL
DLL Diff
17
19
21
23
3
4
5
6
7

Figure 9.

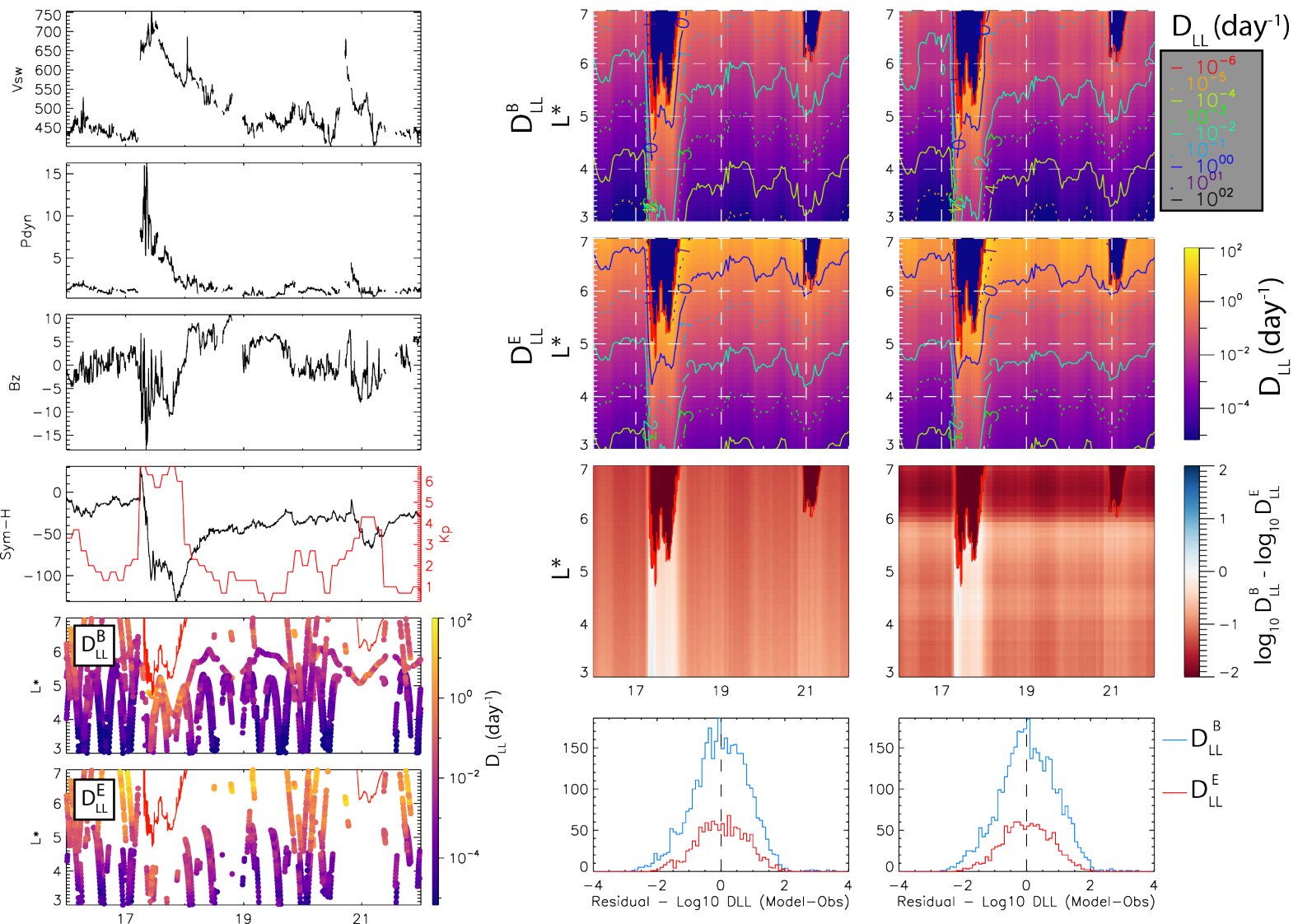
Vsw
Pdyn
Bz
Sym−H
Kp
L*
D_{LL}^{B}
D_{LL}^{E}
D_{LL} (day^{-1})
$\log_{10} D_{LL}^{B} - \log_{10} D_{LL}^{E}$
Residual = Log10 DLL (Model−Obs)

Figure 10.

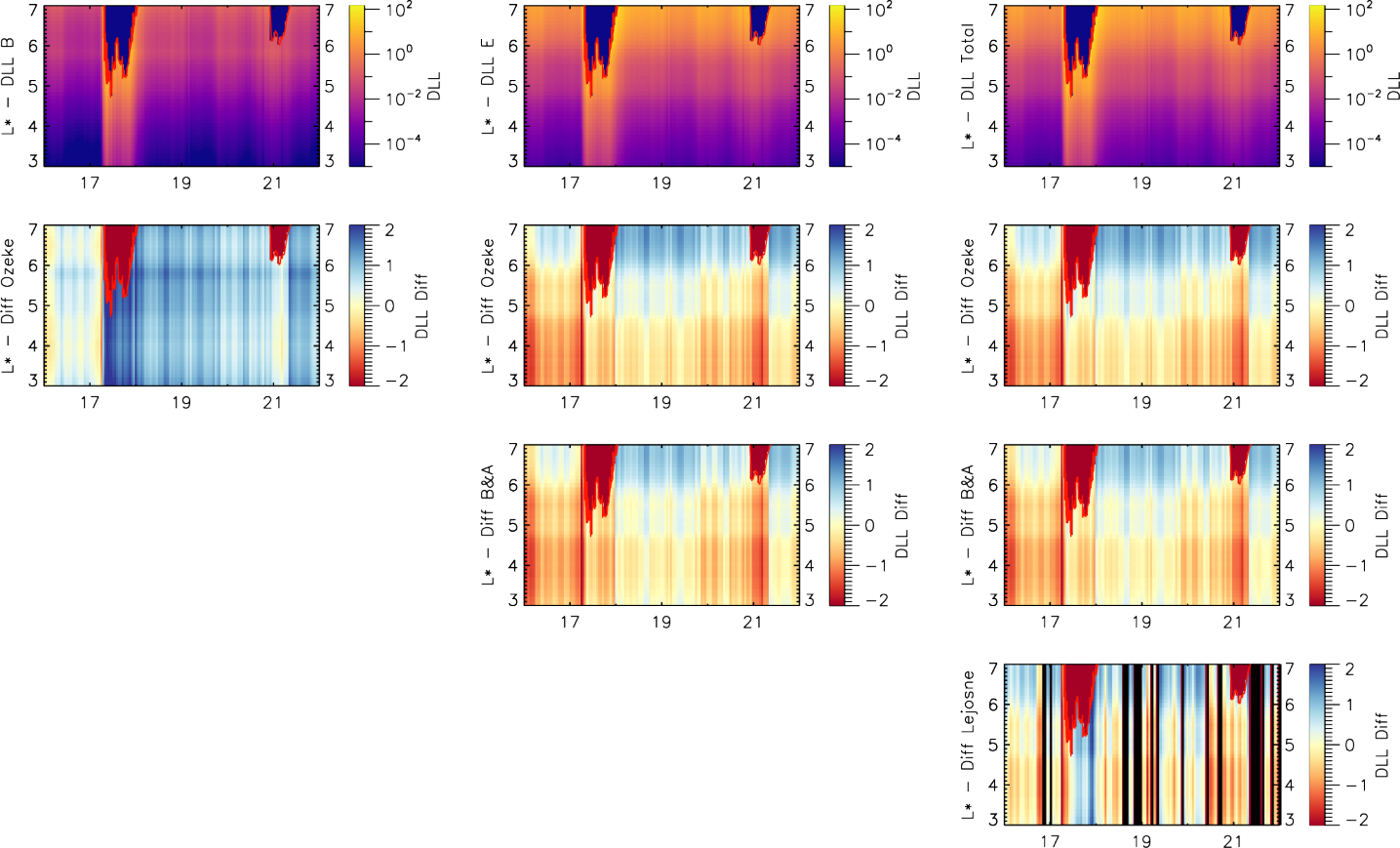
L* – DLL B
L* – DLL E
L* – DLL Total
DLL
L* – Diff Ozeke
L* – Diff B&A
L* – Diff Lejosne
DLL Diff
17
19
21
3
4
5
6
7